BAMS Article

Utilizing a Storm-Generating Hotspot to Study Convective Cloud Transitions

The CACTI Experiment

SPECIAL RELAMPAGO-CACTI COLLECTION

Adam C. Varble, Stephen W. Nesbitt, Paola Salio, Joseph C. Hardin, Nitin Bharadwaj, Paloma Borque, Paul J. DeMott, Zhe Feng, Thomas C. J. Hill, James N. Marquis, Alyssa Matthews, Fan Mei, Rusen Öktem, Vagner Castro, Lexie Goldberger, Alexis Hunzinger, Kevin R. Barry, Sonia M. Kreidenweis, Greg M. McFarquhar, Lynn A. McMurdie, Mikhail Pekour, Heath Powers, David M. Romps, Celeste Saulo, Beat Schmid, Jason M. Tomlinson, Susan C. van den Heever, Alla Zelenyuk, Zhixiao Zhang, and Edward J. Zipser

ABSTRACT: The Cloud, Aerosol, and Complex Terrain Interactions (CACTI) field campaign was designed to improve understanding of orographic cloud life cycles in relation to surrounding atmospheric thermodynamic, flow, and aerosol conditions. The deployment to the Sierras de Córdoba range in north-central Argentina was chosen because of very frequent cumulus congestus, deep convection initiation, and mesoscale convective organization uniquely observable from a fixed site. The C-band Scanning Atmospheric Radiation Measurement (ARM) Precipitation Radar was deployed for the first time with over 50 ARM Mobile Facility atmospheric state, surface, aerosol, radiation, cloud, and precipitation instruments between October 2018 and April 2019. An intensive observing period (IOP) coincident with the RELAMPAGO field campaign was held between 1 November and 15 December during which 22 flights were performed by the ARM Gulfstream-1 aircraft. A multitude of atmospheric processes and cloud conditions were observed over the 7-month campaign, including numerous orographic cumulus and stratocumulus events; new particle formation and growth producing high aerosol concentrations; drizzle formation in fog and shallow liquid clouds; very low aerosol conditions following wet deposition in heavy rainfall; initiation of ice in congestus clouds across a range of temperatures; extreme deep convection reaching 21-km altitudes; and organization of intense, hail-containing supercells and mesoscale convective systems. These comprehensive datasets include many of the first ever collected in this region and provide new opportunities to study orographic cloud evolution and interactions with meteorological conditions, aerosols, surface conditions, and radiation in mountainous terrain.

KEYWORDS: Convective clouds; Precipitation; Storm environments; In situ atmospheric observations; Remote sensing; Aerosol-cloud interaction; Aerosols/particulates; Aircraft observations; Boundary layer; Clouds; Complex terrain; Convective storms; Convective-scale processes; Cumulus clouds; Deep convection; Diurnal effects; Drizzle; Extreme events; Field experiments; Fog; Hail; Instability; Instrumentation/sensors; Lidars/Lidar observations; Longwave radiation; Measurements; Mesoscale processes; Mesoscale systems; Microwave observations; Mountain meteorology; Orographic effects; Profilers; atmospheric; Radars/Radar observations; Radiative fluxes; Radiosonde/rawinsonde observations; Rainfall; Satellite observations; Severe storms; Shortwave radiation; Soil moisture; Soil temperature; Soundings; South America; Southern Hemisphere; Stratiform clouds; Subseasonal variability; Supercells; Surface fluxes; Surface observations; Thunderstorms; Topographic effects; Valley/mountain flows; Wind profilers; Wind shear

https://doi.org/10.1175/BAMS-D-20-0030.1

Corresponding author: Adam Varble, adam.varble@pnnl.gov

In final form 19 March 2021

©2021 American Meteorological Society
For information regarding reuse of this content and general copyright information, consult the AMS Copyright Policy.

AFFILIATIONS: Varble—Atmospheric Sciences and Global Change Division, Pacific Northwest National Laboratory, Richland, Washington, and Department of Atmospheric Sciences, University of Utah, Salt Lake City, Utah; **Nesbitt**—Department of Atmospheric Sciences, University of Illinois at Urbana–Champaign, Urbana, Illinois; **Salio**—Centro de Investigaciones del Mar y la Atmósfera, Instituto Franco-Argentino para el Estudio del Clima y sus Impactos, Universidad de Buenos Aires, Buenos Aires, Argentina; **Hardin, Borque, Feng, Marquis, Matthews, Mei, Goldberger, Hunzinger, Pekour, Schmid, Tomlinson, and Zelenyuk**—Atmospheric Sciences and Global Change Division, Pacific Northwest National Laboratory, Richland, Washington; **Bharadwaj**—Atmospheric Sciences and Global Change Division, Pacific Northwest National Laboratory, Richland, Washington, and Fortem Technologies, Pleasant Grove, Utah; **DeMott, Hill, Barry, Kreidenweis, and van den Heever**—Department of Atmospheric Science, Colorado State University, Fort Collins, Colorado; **Öktem and Romps**—Department of Earth and Planetary Science, University of California, Berkeley, and Climate and Ecosystem Sciences Division, Lawrence Berkeley National Laboratory, Berkeley, California; **Castro**—Universidade dos Açores, Ponta Delgada, Portugal; **McFarquhar**—Cooperative Institute for Mesoscale Meteorological Studies, and School of Meteorology, University of Oklahoma, Norman, Oklahoma; **McMurdie**—Department of Atmospheric Sciences, University of Washington, Seattle, Washington; **Powers**—Los Alamos National Laboratory, Los Alamos, New Mexico; **Saulo**—Servicio Meteorológico Nacional, Buenos Aires, Argentina; **Zhang and Zipser**—Department of Atmospheric Sciences, University of Utah, Salt Lake City, Utah

The U.S. Department of Energy (DOE) Atmospheric Radiation Measurements (ARM) Cloud, Aerosol, and Complex Terrain Interactions (CACTI) field campaign was recently completed over a 7-month period from October 2018 through April 2019 in the Sierras de Córdoba (SDC) range of central Argentina. A primary goal was to use the high frequency of orographically initiated convective clouds to comprehensively study the complex interactions between meteorology, aerosols, complex terrain, and convective cloud life cycles. This article summarizes the campaign while highlighting ongoing and potential future research using its unique datasets.

Complex terrain provides a natural laboratory to study a range of cloud types and processes because of how frequently clouds anchor to specific topographic features. These features often strongly impact atmospheric circulations that commonly affect cloud and thunderstorm formation (Houze 2012). Many mountainous regions of the world exert a primary control on the initiation of deep convection that often grows upscale into mesoscale convective systems (MCSs), producing a majority of rainfall downstream of these regions (e.g., Laing and Fritsch 1997; Nesbitt et al. 2006; Durkee et al. 2009).

Poor prediction of deep convection initiation timing and location (e.g., Dai 2006), upscale growth from isolated to mesoscale systems (e.g., Hohenegger and Stevens 2013; Hagos et al. 2014), propagation (e.g., Del Genio et al. 2012; Song et al. 2013), and surface flux–precipitation interactions (e.g., Taylor et al. 2012; Klein and Taylor 2020; Qian et al. 2020) likely contribute to a warm, dry bias in climate models downstream of the SDC range (Carril et al. 2012; Solman et al. 2013) and other mountain ranges such as the Rockies (Anderson et al. 2003; Klein et al. 2006), which are key agricultural regions. Increasing model resolution has improved predictions, but even models without parameterized deep convection tend to display overly strong updrafts (Varble et al. 2014a; Marinescu et al. 2016; Fan et al. 2017), excessive riming that results in high-biased radar reflectivity (e.g., Lang et al. 2011; Varble et al. 2011; Fridlind et al. 2012; Stanford et al. 2017), and low-biased stratiform rainfall (e.g., Hagos et al. 2014; Varble et al. 2014b; Han et al. 2019). Improving the representation of these systems as a function of environmental conditions in multiscale models will help to answer the question of how water and food resources will change in a changing climate. Recent experiments including CuPIDO (Damiani et al. 2008), COPS (Wulfmeyer et al. 2008), and DOMEX (Smith et al. 2012)

have sought to better understand orographic cumulus and deep convective cloud life cycles. While these and many other non-orographic campaigns have contributed substantially to our understanding of interactions between clouds and their surrounding environment, sampling limitations have left open critical questions.

The wide range of environmental conditions in central Argentina and the high frequency of orographic convective clouds that evolve into deeper congestus, initiate into deep convection (Rasmussen and Houze 2011, 2016; Mulholland et al. 2018), and organize into mesoscale systems near the SDC range (Anabor et al. 2008; Romatschke and Houze 2010; Rasmussen et al. 2014, 2016) make it an ideal location to quantify interactions between convective clouds and their surrounding environment. Extreme storms in Argentina stand out as being some of the world's deepest (Zipser et al. 2006), largest (Velasco and Fritsch 1987), and longest-lived (Durkee and Mote 2009) with some of the highest lightning flash rates (Cecil et al. 2015) and largest hail (Cecil and Blankenship 2012; Kumjian et al. 2020) on Earth. The convective life cycle in this region is significantly influenced by orographic flows (Nicolini and Skabar 2011; Rasmussen and Houze 2011; Bueno Repinaldo et al. 2015; Mulholland et al. 2019, 2020), the South American low-level jet (Nicolini et al. 2002; Salio et al. 2002, 2007; Saulo et al. 2004, 2007; Borque et al. 2010), and synoptic-scale troughs that induce the Northwestern Argentinean ("Chaco") low (Seluchi et al. 2003), free-tropospheric subsidence (Ribeiro and Bosart 2018), eastward-propagating drylines (Bechis et al. 2020), and northward-propagating cold fronts (Seluchi et al. 2006) east of the Andes. Changes in land surface properties throughout the October–April warm season during which most precipitation falls impact surface fluxes and boundary layer evolution on daily and seasonal time scales that feed back to cloud and rainfall generation (e.g., Saulo et al. 2010; Sörensson and Menéndez 2011; Ruscica et al. 2015). Finally, local and long-range transport of biomass-burning smoke (Freitas et al. 2005; Camponogara et al. 2014, Della Ceca et al. 2018) and blowing dust impact aerosol properties in the region (Winker et al. 2013), but much remains unknown because of limited measurements in the region.

Objectives

The unique atmospheric conditions of central Argentina coupled with the motivation to better understand two-way interactions between convective clouds and their surrounding environment motivated the CACTI field campaign. The experiment was designed to address the following primary science questions:

1) How do orographically generated cumulus humilis, mediocris, and congestus clouds interact with and depend on environmental flows, thermodynamics, aerosols, and surface properties?
2) What combinations of environmental conditions promote or suppress deep convection initiation, upscale growth, and mesoscale organization, and how do deep convective systems alter surface and aerosol properties?

This multifaceted experiment involved deployment or an ARM mobile facility (AMF1; Mather and Voyles 2013) and the C-band Scanning ARM Precipitation Radar (C-SAPR2) for a long-term 6.5-month Extended Observing Period (15 October 2018–30 April 2019), and a 1.5-month intensive observation period (IOP; 1 November–15 December 2018) that included Gulfstream-1 (G-1) aircraft flights. The campaign overlapped with the collaborating multi-agency, National Science Foundation (NSF)-led Remote Sensing of Electrification, Lightning, and Mesoscale/Microscale Processes with Adaptive Ground Observations (RELAMPAGO) field campaign [see companion article by Nesbitt et al. (2021)].

The processes targeted by CACTI measurements are shown in Fig. 1. One goal was to measure impacts of boundary layer evolution, orographic thermal and mechanical flows, occasional northerly low-level jets, and free-tropospheric conditions on the evolution of orographic cumulus, stratocumulus, and deeper convective clouds. North–south–oriented orographic cumulus cloud lines formed most frequently to the west of the AMF1 site over or just east of the highest terrain, fed by air east of the SDC when clouds were coupled with the boundary layer. Free-tropospheric flow typically had a westerly component, causing congestus clouds to shear toward the AMF1. In these situations, a primary goal was to measure the cloud-base inflow aerosol and thermodynamic properties while retrieving evolving properties of clouds and detrained air aloft through remote sensing, radiosondes, and the G-1. A second goal was to measure processes associated with the formation of rain and ice in convective clouds that led to deep convection initiation, in addition to processes that promoted or suppressed deep convective upscale growth into mesoscale complexes, for example through cold pool outflow interactions with the complex terrain and ambient atmospheric conditions. A third goal involved measurement of the impacts of clouds and precipitation on free-tropospheric thermodynamics, aerosol wet deposition, and surface moistening, and how these impacts affected subsequent clouds.

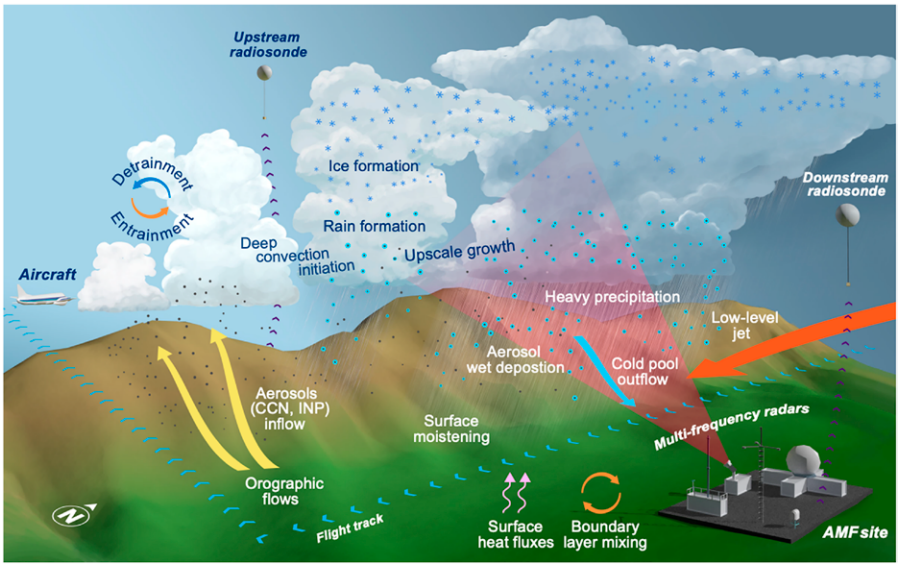

Fig. 1. A conceptual rendering of the atmospheric processes targeted by CACTI with some of the critical observing platforms.

Observational strategy

Ground deployment. The AMF1 with over 50 instruments was deployed with the C-SAPR2 to a rural location at 1,141-m elevation just east of Villa Yacanto, Argentina. The location was on the eastern slopes of the SDC, about 20 km from the primary north–south-oriented ridgeline crest that rises 2,000 m above the surrounding plains (Fig. 2). Radar beam blockage was minimal apart from the lowest levels to the west where the higher terrain was located. The AMF1 was also well offset from anthropogenic aerosol sources to the northeast where the prevailing flow originated. Views of the site are shown in Fig. 3. Additional sites included a second sounding

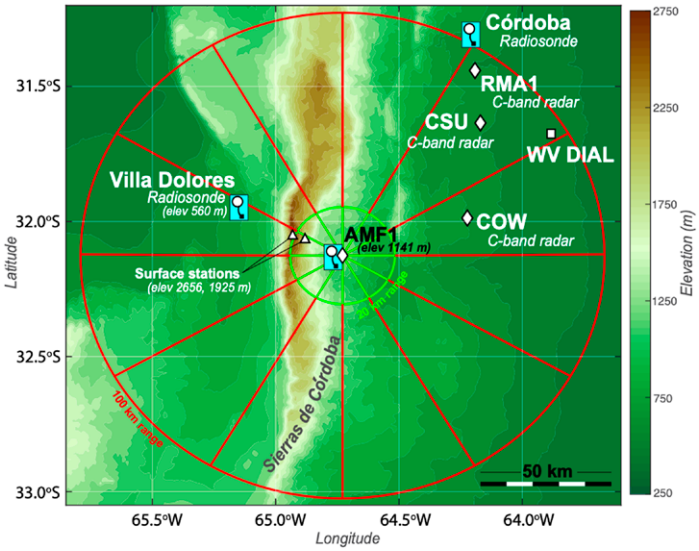

Fig. 2. A map of the CACTI observing domain highlighting the Sierras de Córdoba range, the AMF1 site, high-elevation meteorological stations, and the second sounding site. Hemispheric RHIs were performed by the scanning radars along the radials shown. The Argentine operational RMA1 C-band radar and Córdoba sounding sites, and fixed RELAMPAGO C-band radar and differential absorption lidar (WV DIAL) sites, are also shown.

and meteorological station at Villa Dolores Airport west of the mountains, two high-elevation meteorological stations between the AMF1 and Villa Dolores sites, and camera sites offset 1–2 km from the AMF1 for stereo photogrammetry. Figure 2 also shows operational Córdoba sounding and radar sites, and fixed RELAMPAGO sites where C-band radars and a differential absorption lidar were deployed for a portion of CACTI.

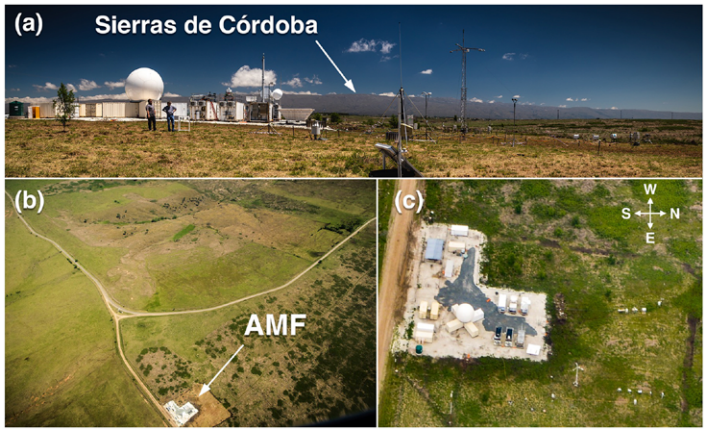

Fig. 3. (a) A view west across the AMF1 site toward the crest of the Sierras de Córdoba range. Aerial views of the AMF1 site (b) looking toward the northwest and (c) zoomed in on the site.

The extensive ground instrumentation deployed for CACTI and their primary measurements are shown in Table 1. Although the campaign officially began 15 October, most measurements began in late September. Scanning Ka-, X-, and C-band radars and a vertically pointing Ka-band radar made critical cloud and precipitation measurements. The radar scan strategy targeted the evolution of close by convective clouds. The C-SAPR2 performed a 15-tilt plan position indicator (PPI) "volume" between elevation angles of 0.5° and 33° followed by a vertically pointing, azimuthally rotating ("bird bath") ZPPI, and two six-azimuth hemispheric range–height indicator (HSRHI) patterns along the radials shown in Fig. 2. Hemispheric (HS) in this context refers to scanning from one horizon to the other (180° in elevation) at a constant azimuth. This sequence was repeated every 15 min. The X-/Ka-band Scanning ARM Cloud Radar (SACR) also performed a 15-min sequence with a 30°-wide sector RHI scan between west-southwest and west, followed by the HSRHI pattern repeated three times. The sector RHI was performed because four HSRHI patterns could not be comfortably fit into a 15-min sequence, but it also provides a limited volume with high vertical resolution within the field of view of stereo cameras from which cloud boundary retrievals are possible.

Periods of C-SAPR2 pedestal mechanical issues began in late December, and by early March, the azimuthal motor failed. At this time, the C-SAPR2 was reconfigured to perform a west–east HSRHI pattern with 45-s updates for the rest of the campaign. The X/Ka-SACR then began performing PPI volumes, replacing the sector RHI and one of the HSRHI patterns in each 15-min sequence. These volumes had a shorter range (60 vs 110 km), lower angular resolution, and greater attenuation in heavy precipitation than C-SAPR2 volumes but filled the PPI volume gap for the rest of the campaign.

Additional cloud and precipitation measurements were continuously made by disdrometers, rain gauges, cameras, microwave radiometers, lidars, and a total-sky imager. Radiosondes were the most critical instrument for measuring atmospheric state. At the AMF1 site, they were launched every 3–4 h between 0900 and 2100 local time (LT) (1200 and 0000 UTC). The sounding site at Villa Dolores launched at 0900 and 1500 LT (1200 and 1800 UTC). Additional atmospheric kinematic and thermodynamic information was provided by surface meteorological stations, microwave radiometers, an Atmospheric Emitted Radiation Interferometer, a Doppler lidar, a radar wind profiler, and a sodar. Surface conditions were monitored with eddy correlation flux measurement and surface energy balance systems. Exhaustive spectral and broadband, upwelling and downwelling, shortwave and longwave radiation measurements were made by a number of radiometers. Last, comprehensive aerosol scattering, absorption, size distribution, and chemical composition measurements were made along with concentrations of condensation nuclei, cloud condensation nuclei at several supersaturations, ice nucleating particles, and several trace gases.

Table 1. Ground instrumentation deployed with primary measurements provided by instrumentation. Refer to Varble et al. (2019) for notes on data quality.

Ground-based instruments and measurements	
Cloud and precipitation measurements	**Instrumentation**
Cloud and precipitation kinematic and microphysical retrievals	C-band scanning ARM precipitation radar, Ka-/X-band scanning ARM cloud radar, Ka-band ARM zenith radar, radar wind profiler
Heights of cloud bases/tops, sizes, and vertical winds	ARM cloud digital cameras
Cloud-base height	Ceilometer, micropulse lidar, Doppler lidar
Cloud scene/fraction	Total-sky imager
Raindrop size distribution, fall speeds, and rainfall	Parsivel laser and 2D video disdrometers, tipping- and weighing-bucket rain gauges, optical rain gauge, present weather detector
Liquid water path	Two-channel, high-frequency, and profiling microwave radiometers
Atmospheric-state measurements	**Instrumentation**
Precipitable water	Two-channel, high-frequency, and profiling microwave radiometers
Surface pressure, temperature, humidity, winds, and visibility	Surface meteorological stations (four sites)
Vertical profiles of temperature, humidity, and winds	Radiosondes (two sites), radar wind profiler, profiling microwave radiometer, atmospheric emitted radiation interferometer
Boundary layer winds and turbulence	Doppler lidar, sodar
Surface-condition measurements	**Instrumentation**
Surface heat fluxes and energy balance, CO_2 flux, turbulence, and soil temperature and moisture	Eddy correlation flux measurement system, surface energy balance system
Aerosol and trace-gas measurements	**Instrumentation**
Aerosol backscatter profile	Micropulse lidar, Doppler lidar, Ceilometer
Aerosol optical depth	Cimel sun photometer, multifilter rotating shadowband radiometer
Cloud condensation nuclei (CCN) concentration	Dual-column CCN counter
Condensation nuclei (CN) concentration	Fine and ultrafine condensation particle counters
Ice nucleating particle (INP) concentration	Filters processed in Colorado State University Ice Spectrometer
Aerosol chemical composition	Aerosol chemistry speciation monitor, single-particle soot photometer
Aerosol scattering and growth	Ambient and variable humidity nephelometers
Aerosol absorption	Particle soot absorption photometer
Aerosol size distribution	Ultrahigh sensitivity aerosol spectrometer, scanning mobility particle sizer, aerodynamic particle sizer
Trace-gas concentrations	O_3, CO, N_2O, H_2O monitoring systems
Radiation measurements	**Instrumentation**
Radiative fluxes	Broadband direct, diffuse, and total downwelling radiation radiometers; broadband upwelling radiation radiometers; ground and sky infrared thermometers; AERI; narrow field of view two-channel zenith radiometer; hemispheric and zenith shortwave array spectroradiometers; multifilter radiometer; multifilter rotating shadowband radiometer; Cimel sun photometer; surface energy balance system; two-channel, high-frequency, and profiling microwave radiometers

Aircraft deployment. The G-1 (Schmid et al. 2014) completed 22 flights between 4 November and 8 December totaling 79.4 h of flight time (Fig. 4). The instrumentation payload and measurements made are shown in Table 2, and each flight is described in Table 3. Nineteen flights sampled cumulus humulis, cumulus congestus, or stratocumulus clouds, with most having clear ties to the topography, while eight included initiation of deep convection during or shortly after flights. Flight summaries can be downloaded on the RELAMPAGO field catalog available through the National Center for Atmospheric Research Earth Observing Laboratory

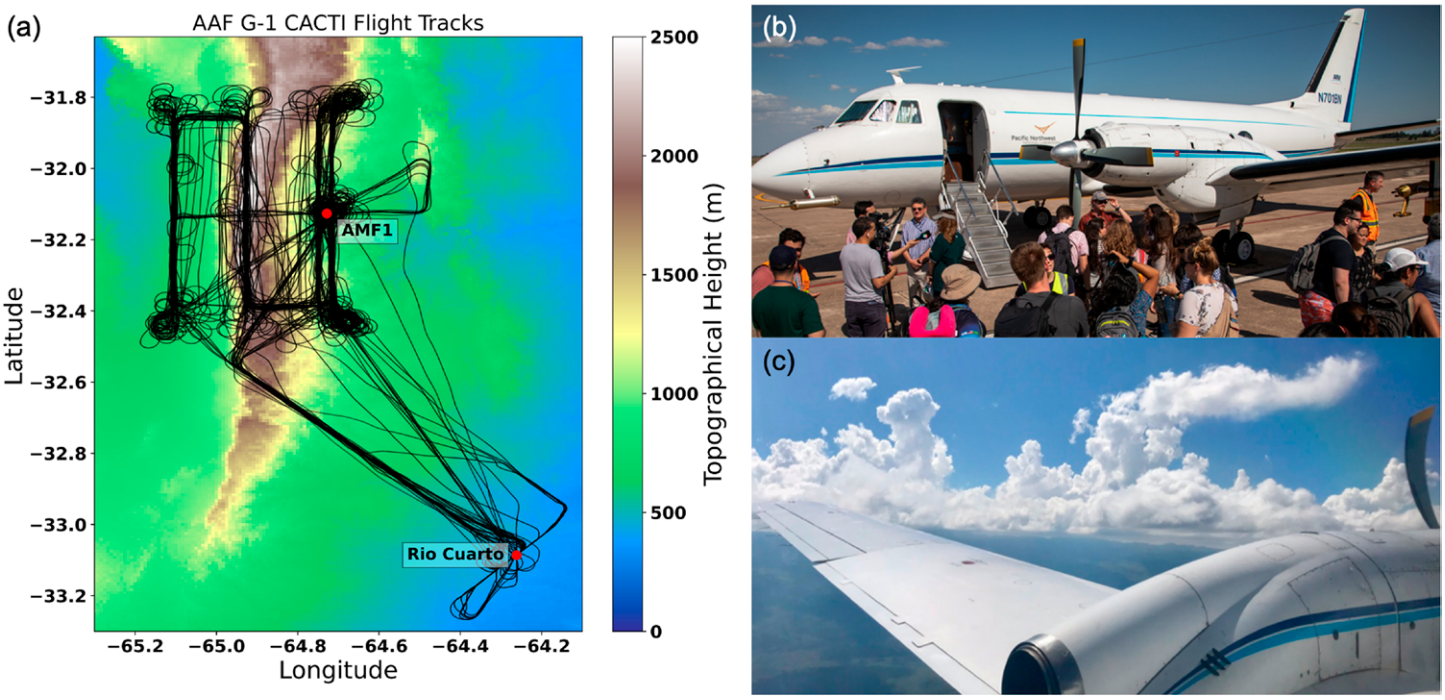

Fig. 4. (a) A map overlaid with the 22 flight tracks, (b) an outreach event on 15 Nov 2018, and (c) cumulus congestus with ice formation from flight 10 on 21 Nov 2018.

Table 2. G-1 aircraft instrumentation during CACTI with primary measurements of each instrument. Please see Varble et al. (2019) for data quality notes.

Aircraft instruments and measurements	
Positioning measurements	**Instrumentation**
Position/aircraft parameters	Aircraft-integrated meteorological measurement system-20, global positioning system (GPS) DSM 232, C-MIGITS III (miniature integrated GPS/INS tactical system), VectorNav-200 GPS/INS, Video Camera P1344
Atmospheric-state measurements	**Instrumentation**
Pressure, temperature, humidity, winds, and turbulence	Gust Probe, Rosemount 1221F2, Aircraft Integrated Meteorological Measurement System-20, Tunable Diode Laser Hygrometer, GE-1011B Chilled Mirror Hygrometer, Licor LI-840A, Rosemount 1201F1 and E102AL
Aerosol and trace-gas measurements	**Instrumentation**
Aerosol sampling	Aerosol Isokinetic Inlet, Counterflow Virtual Impactor (CVI) Inlet
Aerosol optical properties	Single particle soot photometer, three-wavelength integrating nephelometer, three-wavelength particle soot absorption photometer, three-wavelength single-channel tricolor absorption photometer
Aerosol chemical composition	Single-particle mass spectrometer (miniSPLAT)
Aerosol size distribution	Ultrahigh sensitivity aerosol spectrometer, scanning mobility particle sizer, passive cavity aerosol spectrometer, optical particle counter model CI-3100, dual-polarized cloud and aerosol spectrometer (CAS)
CN concentration	Fine (1 on Isokinetic Inlet and 1 on CVI Inlet) and Ultrafine CPCs
CCN concentration	Dual-column CCN counter
INP concentration	Filter collections for Colorado State University Ice Spectrometer
Trace-gas concentrations	N_2O, CO, O_3, and SO_2 monitoring systems
Cloud and precipitation measurements	**Instrumentation**
Hydrometeor size distribution	Fast Cloud Droplet Probe, two-dimensional stereo probe, High Volume Precipitation Sampler 3, Cloud and Aerosol Precipitation Spectrometer (CAPS; includes Cloud Imaging Probe, CAS, and Hotwire Sensor)
Hydrometeor imagery	Cloud particle imager
Liquid water content	Particle volume monitor 100-A, multi-element water content meter, Hotwire Sensor from CAPS

Table 3. CACTI G-1 flights including their date, time, and situation. Flight summaries can be downloaded from the RELAMPAGO field catalog hosted by NCAR EOL.

Flight	Time and date	Situation
1	1302–1701 UTC 4 Nov	Deepening orographic cumulus
2	1309–1705 UTC 6 Nov	Deep convection initiation; likely warm rain
3	1210–1610 UTC 10 Nov	Deepening orographic cumulus prior to deep convection initiation
4	1648–2000 UTC 12 Nov	Elevated deep convection, low-level stable cumulus and stratus
5	1400–1800 UTC 14 Nov	Clear-air aerosol sampling
6	1305–1600 UTC 15 Nov	Clear-air aerosol sampling
7	1405–1800 UTC 16 Nov	Boundary layer and elevated orographic cumulus
8	1218–1630 UTC 17 Nov	Congestus along cold front; wind-blown dust; mountain wave
9	1510–1906 UTC 20 Nov	Orographic cumulus; strong inversion
10	1822–2027 UTC 21 Nov	Orographic congestus and deep convection initiation
11	1431–1811 UTC 22 Nov	Stratiform anvil sampling along radar north–south scans
12	1617–2025 UTC 24 Nov	Orographic cumulus line; strong inversion
13	1551–1907 UTC 25 Nov	Orographic cumulus line; potential decoupling from boundary layer
14	1508–1850 UTC 28 Nov	Orographic congestus and deep convection initiation
15	1416–1632 UTC 29 Nov	Orographic congestus and deep convection initiation
16	1620–1847 UTC 1 Dec	Elevated drizzle in orographic stratocumulus; possible ice
17	1206–1611 UTC 2 Dec	Elevated drizzle in widespread clouds; possible ice; gravity waves in cloud layer
18	1603–2009 UTC 3 Dec	Boundary layer coupled orographic cumulus; strong inversion
19	1751–1945 UTC 4 Dec	Deepening congestus and some deep convection initiation
20	1204–1528 UTC 5 Dec	Midlevel clouds; congestus and some deep convection initiation
21	1501–1901 UTC 7 Dec	Orographic cumulus; strengthening inversion
22	1606–1930 UTC 8 Dec	Clear-air aerosol sampling

(NCAR EOL; catalog.eol.ucar.edu/relampago). Aircraft position and atmospheric-state measurements with 1–100-Hz sampling were made by a number of instruments. Comprehensive aerosol measurements overlapped significantly with measurements made continuously at the surface AMF1 site and included aerosol scattering and absorption, size distribution, and chemical composition in addition to condensation nuclei, cloud condensation nuclei, ice nucleating particle, and trace-gas concentrations. In situ cloud properties measured included bulk condensed water content from several sensors, a cloud particle imager, and hydrometeor size distributions.

Most flights performed north–south, constant-altitude legs over the AMF site, over the highest terrain where clouds were most frequent, and to the west of the clouds and highest terrain (Fig. 4). Legs were flown just below cloud base (when possible), at midcloud level through cloud and to its west and east, and at cloud top, repeating in time. Some flights also included a spiral down over the AMF site to provide an aerosol and thermodynamic profile. Deviations from this strategy were performed on occasion based on meteorological or cloud conditions. The aerosol isokinetic inlet was used to sample the clear sky aerosol population above, below, and adjacent to clouds. The counterflow virtual impactor (CVI) inlet was used for in-cloud sampling, to characterize cloud droplet residuals, and compare their sizes and compositions to particles outside clouds.

Coordination with the RELAMPAGO field campaign. CACTI coincided with the RELAMPAGO field campaign [see companion article by Nesbitt et al. (2021)] which included a hydrologic

component from June 2018 through April 2019 and an IOP between November 2018 and January 2019. RELAMPAGO and CACTI teams coordinated operations due to their shared goals of targeting initiating and growing deep convective clouds. The CACTI PI and some science team members were commonly located with the RELAMPAGO science team at the RELAMPAGO operations center in Villa Carlos Paz. Forecasts and near-real-time data displays utilized for RELAMPAGO mobile missions were also utilized for the adaptive observing components of CACTI during the IOP. During RELAMPAGO mobile missions, the CACTI observing sites were commonly used as part of the RELAMPAGO observing network.

The integration of these two campaigns has resulted in synergistic usage of data from RELAMPAGO and CACTI instrumentation for a number of studies. For example, RELAMPAGO radar measurements are being used with C-SAPR2 for multi-Doppler retrieved boundary layer and cloud dynamics during initiating and growing deep convection (Marquis et al. 2021) within the dense RELAMPAGO radiosonde networks during mobile missions. These well-sampled, better-characterized RELAMPAGO IOP cases will contextualize the many additional cases observed during CACTI, while CACTI radar rain-rate retrievals will help contextualize the long-term RELAMPAGO hydrologic observations.

Operations and outreach

Most CACTI instruments operated continuously and were monitored by ARM site technicians and engineers; however, some measurements were adjusted in response to weather forecasts or real-time observations. During the IOP, forecasts were provided by members of Servicio Meteorológico Nacional (SMN) and graduate students. Forecasts typically used global numerical weather prediction and regional convection-allowing model guidance that was run every 6–12 h by SMN, the University of Illinois, and Colorado State University (CSU). When deep convection was forecasted, AMF1 radiosonde launch frequency was increased from 4- to 3-hourly between 0900 and 2100 LT. Additional sondes were also occasionally launched from the Villa Dolores site. In addition, *Geostationary Operational Environmental Satellite-16* (*GOES-16*) mesoscale domain sectors (MDSs) with 1-min updates were requested from the National Oceanic and Atmospheric Administration (NOAA) on these days with most requests granted. These data are available from the NOAA Comprehensive Large Array-Data Stewardship System (CLASS; www.class.noaa.gov). Outside of the IOP, model forecast guidance was used to coordinate daily radiosonde launch schedules and MDS requests. In addition, during select IOP daytime periods, the C-SAPR2 HSRHI radar scans were modified on site to target specific convective cells with sector RHIs.

Forecasts also informed flight planning for the next day, which consisted of a pattern and takeoff time that were decided upon by the PI, G-1 manager, and lead pilot on site in Río Cuarto. Updated forecasts and real-time conditions were checked at least 4 h prior to takeoff to determine whether the flight takeoff should be delayed based on unexpected conditions. While airborne, G-1 flights were monitored in real time with radar, satellite, lightning, and flight track displays at the RELAMPAGO operations center. The lead flight scientist would communicate with the PI to adjust flight legs and updates were sent if inclement weather approached the flight operating area. Debriefs followed each flight, and mission summaries were written and uploaded to the RELAMPAGO field catalog.

Outreach efforts were performed by team members and ARM staff, facilitated by Investigación Aplicada (INVAP S.E.), who helped to manage CACTI. Prior to the start of CACTI, Paola Salio performed local outreach to explain instrumentation that would be installed just outside of Villa Yacanto. A daylong outreach event was then held at the AMF1 site at the start of the IOP. Members of the public and media were invited along with local high school students to learn about site instrumentation, measurements, operations, and scientific objectives including why the site was chosen and how the science that it would facilitate would benefit future weather and climate prediction in the region. A second outreach event was held at the Río

Cuarto Airport where the G-1 was located. Members of the public, students, the media, airport officials, and governmental officials toured the aircraft and learned about the aircraft measurements and operations component of CACTI. Throughout the campaign, smaller groups of students, scientists, and members of the media were also able to visit the AMF1 site.

Data processing and retrievals

Data collected during CACTI are available through over 200 datastreams within the ARM archive searchable through the DOE ARM CACTI website (www.arm.gov/research/campaigns/amf2018cacti). Over 20 ARM value-added products that combine several datastreams into geophysical retrievals have been completed or are in progress. With ARM VAP names in parentheses, they include quality-controlled radiative flux measurements (RADFLUXANAL), aerosol optical properties (AOP), and corrected surface fluxes (QCECOR). Environmental thermodynamic and kinematic products include planetary boundary layer height estimates from soundings (PBLHT), microwave radiometer retrieved precipitable water (MWRRET), Doppler lidar retrieved horizontal and vertical winds (DLPROF), atmospheric emitted radiance interferometer (AERI)-estimated lower-tropospheric temperature and humidity (AERIOE), interpolated soundings (INTERPSONDE), and variational analysis retrieved large-scale forcing (VARANAL). Cloud products include cloud optical depth (MFRSRCLDOD), combined lidar–radar time–height cloud boundaries (KAZRARSCL), microwave radiometer retrieved liquid water path (MWRRET), radar variables derived from disdrometers (LDQUANTS, VDISQUANTS), Cartesian-gridded multifrequency scanning radar RHIs (KASACRGRIDRHI, XSACRGRIDRHI), and multiscale *GOES-16* cloud retrievals provided by the National Aeronautics and Space Administration (VISST). All radar data collected were calibrated following Hardin et al. (2020) and Hunzinger et al. (2020) using changes in ground clutter signals as a measure of drift relative to absolute calibration measured via corner reflector at a single time.

In addition to data provided by ARM, additional PI products have been or will soon be completed. Aerosol products include ice-nucleating particle (INP) concentrations and composition as a function of temperature processed at CSU from collected surface and aircraft samples, and single particle size and chemical composition aboard the aircraft from the miniSPLAT (Zelenyuk et al. 2010, 2015). Cloud products include stereo camera photogrammetric cloud boundary locations (e.g., Fig. 5; Öktem et al. 2014; Öktem and Romps 2021), *GOES-16* deep convective overshooting top retrievals (Bedka and Khlopenkov 2016), and Cartesian-gridded radar PPI volumes. Higher-level radar products available include those generated by the Taranis radar processing framework including scanning precipitation radar corrections, specific differential phase retrievals, and geophysical retrievals. Geophysical retrievals include hydrometeor identification, rain rate, rainwater content, and mass-weighted mean diameter. These

Fig. 5. An example of stereo photogrammetric-retrieved (a) heights of cloud boundaries, (b) manually tracked growing congestus top tracks, and (c) heights of tracked growing congestus tops in time from 1904 to 1915 UTC 19 Dec 2018.

radar products are being used to develop convective-cell-track and cloud-type databases. All datasets will be made publicly available once published.

Preliminary highlights and research opportunities

Meteorology. Relatively strong upper-level jet westerly flow with variable meridional winds associated with passages of synoptic troughs and ridges was present for most of the campaign even during the summer. Upper-level synoptic troughs crossing the Andes induced the northwestern Argentinean low in the lee of the Andes northwest of the SDC, which would induce northerly low-level flow over the SDC, commonly in the form of a low-level jet. This low-level northerly flow brought moisture from the Amazon into the region while the westerly flow crossing the Andes induced steep free-tropospheric lapse rates and a variable-height inversion layer that allowed low levels to build conditional instability.

SDC topography also modified low-level flow and nearly always had an easterly upslope component, even at night when one might expect surface cooling-induced downslope westerly flow (Fig. 6a). The depth of this easterly flow varied considerably such that the flow at the crest of the SDC at times switched from westerly to easterly and could be above or below inversion layers depending on the situation, as indicated by the location of sharp specific humidity drops in Fig. 6c. Boundary layer northeasterly flow, at times in the form of a low-level jet, was commonly associated with increases in precipitable water (Fig. 6b, black line), specific humidity (Fig. 6c, color fill), and most unstable convective available potential energy (MUCAPE) (Fig. 6c, black line). Following these events, low-level flow often switched to southeasterly, commonly behind MCSs or cold fronts, where stable, moist, and relatively low CCN concentrations supported warm rain formation or drizzling fog. Above this stable

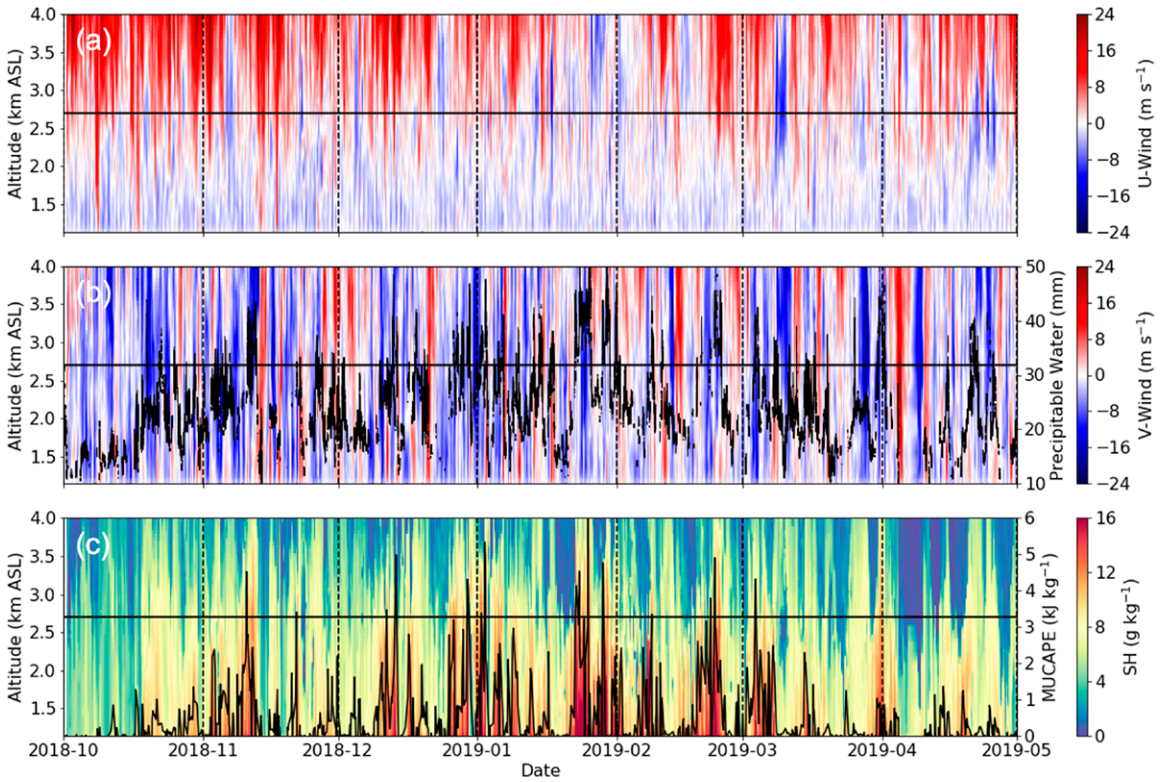

Fig. 6. Low-level (a) zonal wind (positive toward the east), (b) meridional wind (positive toward the north; color fill) with microwave radiometer-retrieved precipitable water (black), and (c) specific humidity (color fill) with radiosonde MUCAPE (black) for the entire campaign from the ARM INTERPOLATEDSONDE product (Fairless and Giangrande 2018). The SDC ridgeline height west of the AMF site is represented by the horizontal black line.

layer, northerly flow commonly continued to advect in warm, moist air, sometimes for a day or more, feeding elevated deep convection decoupled from the surface.

These multiscale circulations supported the presence of CAPE exceeding 100 J kg^{-1} in over 50% of the 935 AMF1 radiosondes launched. Values were often modest but reached extreme values over 6000 J kg^{-1} with levels of neutral buoyancy (LNB, i.e., parcel equilibrium level) exceeding 16 km in January [Fig. 7; see further analyses in Schumacher et al. (2021)]. MUCAPE and LNB most often peaked in the early evening, although most unstable convective inhibition (MUCIN) typically reached a minimum earlier in the afternoon (Fig. 7). MUCAPE parcels originated near the surface about half of the time and thus were frequently elevated off of the surface (Fig. 7) with 30% of soundings with CAPE > 100 J kg^{-1} having most unstable parcels over 1 km above the surface. These conditions appear to be similar to the U.S. Great Plains (e.g., Zhang and Klein 2010). The datasets collected during CACTI provide new opportunities for investigating multiscale atmospheric, surface, and topographic processes that produce commonalities and differences between the moist convection setups in these two regions.

Aerosols. Many aerosol measurements during CACTI were the first ever collected in subtropical South America, providing opportunities to better understand processes that influence their formation, growth, diurnal cycle, and vertical variability within the context of other well observed regions of the world. Figure 8 shows PDFs of observed surface CN and CCN concentrations covering the whole field campaign, highlighting a large spread in values. CN concentrations (>10 nm) were most commonly 1500–2500 cm^{-3} but often extended to higher values that at times exceeded 10^4 cm^{-3}. These higher concentrations are reflected in ~1% supersaturation CCN concentrations that could reach values exceeding 3000 cm^{-3}, although 0.2% CCN concentrations were almost always less than 1000 cm^{-3} and typically much less than that. This highlighted the common occurrence of significant spreads in CCN spectra. Surface CN and CCN concentrations exhibited a distinctive diurnal cycle in which they were minimized around 1200 UTC (0900 LT) and peaked in the early evening (Fig. 8). Contributors to this diurnal variation include afternoon new particle formation and growth, an overnight peak in precipitation, and daytime easterly component boundary layer flows (Fig. 6a). These flows originate from agricultural areas and towns in and along the SDC foothills with the Córdoba metropolitan area of more than 1.5 million people centered

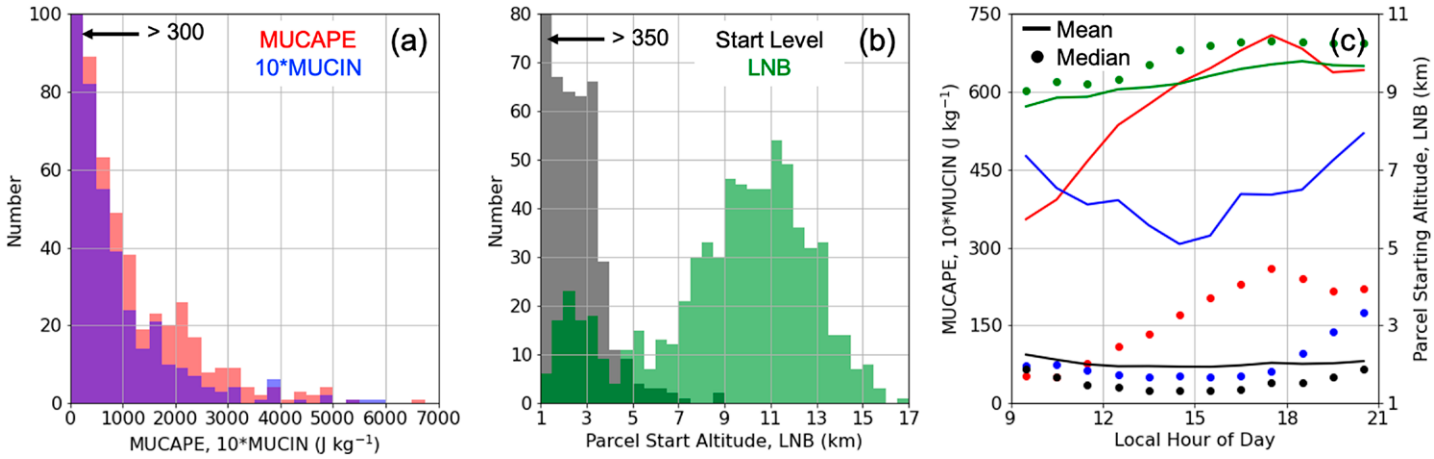

Fig. 7. AMF1 radiosonde (Holdridge et al. 2018) (a) MUCAPE (red) and MUCIN (blue; ×10) PDFs, and (b) MU lifted-parcel starting level (black) and LNB (green) over the entire field campaign between Oct 2018 and Apr 2019. (c) Mean and median MUCAPE (red), MUCIN (blue), MU lifted-parcel starting level (black), and LNB (green) diurnal cycles between 1200 and 0000 UTC (0900 and 2100 LT; the daily period over which sondes were launched every 3–4 h) from INTERPOLATEDSONDE are also shown.

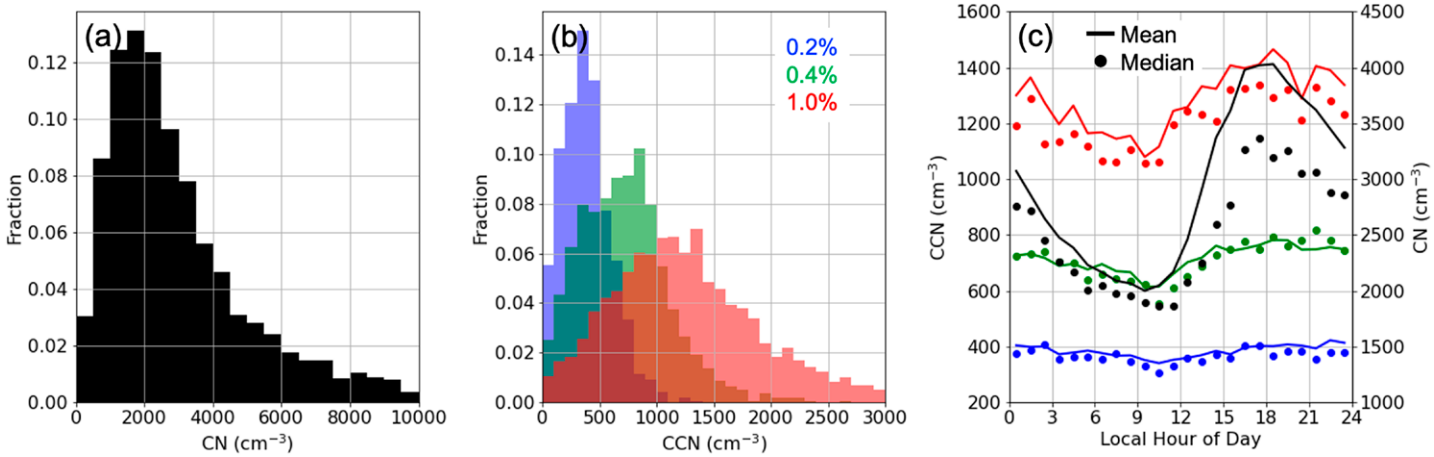

Fig. 8. AMF1 site (a) CN > 10 nm (Kuang et al. 2018a) PDF and (b) CCN (Uin et al. 2018) PDFs colored by supersaturation setpoint (0.2%, 0.4%, and 1.0%) for the entire field campaign between Oct 2018 and Apr 2019. (c) Mean and median CN (black) and CCN (colored by supersaturation) diurnal cycles are also shown.

90 km to the northeast. This mean diurnal cycle is also very similar to that of convective instability shown in Fig. 7.

Comprehensive aerosol size distribution and optical property measurements were also made, both at the surface and aboard the aircraft. The Aerosol Chemistry Speciation Monitor continuously measured mass concentrations of organics, sulfate, nitrate, ammonium, and chloride at the surface, while the miniSPLAT aboard the G-1 measured the size and mixing state of nearly 1.5 million interstitial and cloud droplet residual particles, including particles composed of oxygenated organics mixed with varying amounts of sulfates, organic amines, dust, and fresh and aged soot particles (e.g., Fast et al. 2019). These measurements will be used to better understand how aerosol properties such as chemical composition vary from below cloud to in, around, and above clouds over a range of meteorological and cloud conditions. Such information can also be combined with airmass trajectories to examine local and remote aerosol source regions and how their transport is impacted by complex terrain. For example, ongoing research shows that very high CCN conditions resulted from smoke transport from northeastern Argentina associated with biomass burning (Cancelada et al. 2019).

INP filter samples (DeMott and Hill 2020a,b) were collected on all flights following Levin et al. (2019) and throughout the campaign at the AMF1 site following DeMott et al. (2018a). Collected particles were resuspended in ultrapure water to obtain immersion freezing INP concentrations as a function of temperature using CSU's ice spectrometer (DeMott et al. 2018b). Figure 9 shows all AMF1 spectra collected during the G-1 flight period (17 of 83 in total) compared to the aircraft spectra. Aircraft data agree in form and span with the surface data, although flight-level air often contains fewer INPs at the same temperature. This is likely due to dilution through a well-mixed boundary layer and/or decoupling of flight-level air

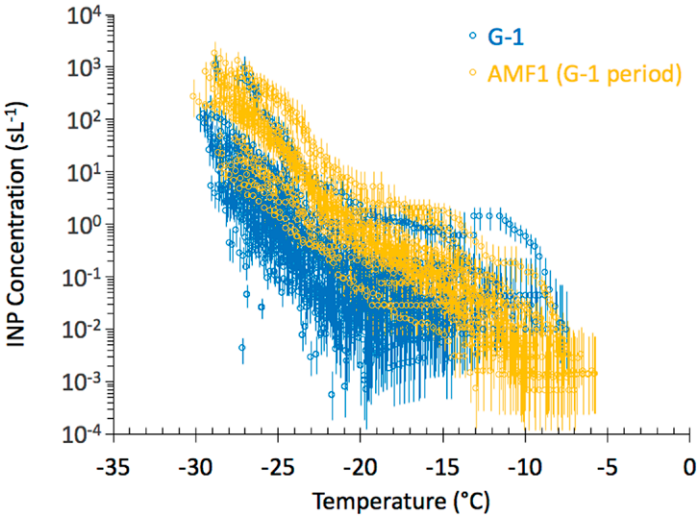

Fig. 9. INP concentrations plotted vs temperature for particles from 34 filters collected on the G-1 and 17 filters collected at the AMF1 site on coincident days (Demott and Hill 2020c,d). Vertical bars represent 95% confidence intervals.

from the surface. The non-log-linear shape of filter spectra, especially the "hump" at temperatures greater than −20°C, indicates a pervasive influence of biological INPs, including bacteria, fungi, and other biomolecules from plants and soils (Hill et al. 2016, 2018, O'Sullivan et al. 2018; Suski et al. 2018). To resolve the microbial/protein, organic, and inorganic INP fractions, INPs were also measured following heating (95°C) and H_2O_2 digestions of aliquots of suspensions (Suski et al. 2018). This INP dataset is the largest collected in subtropical South America, and the data on INP compositions is the most comprehensive for any midlatitude region. Recently completed analyses, being readied for publication, suggest INP source regions primarily from the northeast to southeast of the SDC, with likely important contributions from these sectors' agricultural soils. Comparison with and integration of this new INP dataset with others collected around the world is underway.

Aerosol–cloud–precipitation interactions. The vast array of collocated aerosol, cloud, precipitation, and radiation measurements during CACTI provides unique opportunities for studying aerosol–cloud–precipitation interactions. For surface coupled clouds, the continuous 6.5-month record of meteorological conditions and surface aerosol properties allows for the examination of aerosol direct and indirect effects on shallow cumulus and stratocumulus clouds as well as deeper mixed phase convective clouds. In particular, current research is investigating how CCN concentrations affect stratocumulus rain formation building on Borque et al. (2018), and deep convective cloud microphysical and macrophysical properties building on Varble (2018). In addition, there are opportunities to explore how INPs affect primary ice nucleation in supercooled cumulus congestus clouds.

G-1 measured CN and CCN concentrations varied by two orders of magnitude and often fell significantly between the boundary layer and free troposphere (Fig. 10a). Many cloud measurements were located at 3.1–3.6-km altitudes in orographic cumulus clouds although a range of lower altitude clouds on either side of the SDC were also sampled in addition to deeper congestus clouds. Peak droplet concentrations, typically collected at midcloud altitudes, reached more

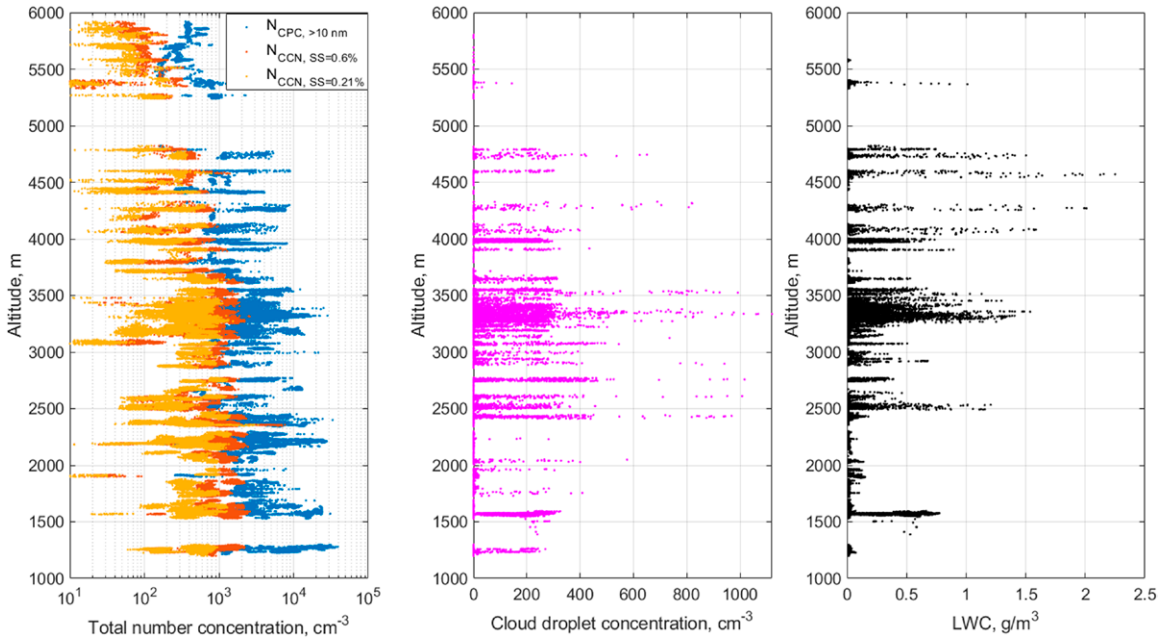

Fig. 10. Cumulative 1-Hz G-1 measurements by altitude of (a) out-of-cloud CN (Mei and Pekour 2018b; blue), 0.21% CCN (Mei and Pekour 2018a; light orange), and 0.6% CCN (dark orange); (b) combined Fast Cloud Droplet Probe, two-dimensional Stereo Probe, and High Volume Precipitation Sampler cloud and rain droplet number concentration (Mei et al. 2018); and (c) Multi-Element Water Content Meter liquid water content (Matthews and Nelson 2018).

than 1000 cm^{-3} but typical values were less than 400 cm^{-3} (Fig. 10b) and often lower than the subcloud 0.2% CCN concentration, indicating potentially lower updraft supersaturations and/or effects of dry-air entrainment. The greatest liquid water contents (LWCs) exceeding 2 g m^{-3} were observed in deep cumulus congestus clouds on 21 November. Most LWCs were much lower in magnitude, although cumulus LWCs occasionally exceeded 1 g m^{-3} (Fig. 10c). Ongoing research is examining linkages between these aerosol and cloud measurements. G-1 measurements can also be used to examine cloud processing of aerosols and vertical transport from lower-altitude, higher-aerosol-loading layers to the relatively cleaner free troposphere.

Surface measurements show many days with new particle formation and growth of aerosols while heavy rainfall events resulted in significant wet deposition. A 1-week example is shown in Fig. 11 via SMPS aerosol size distribution measurements in time. Heavy rainfall on

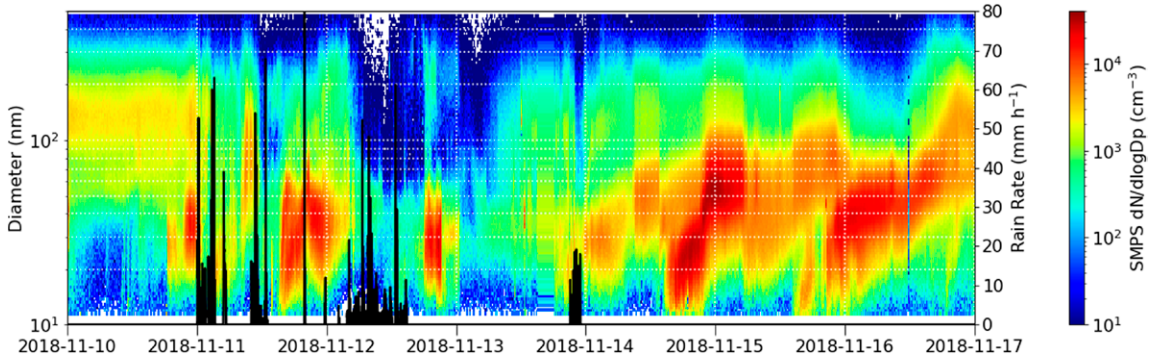

Fig. 11. Surface Scanning Mobility Particle Sizer aerosol size distribution (Kuang et al. 2018b; color fill) with Pluvio-2 1-min rain rate (Wang et al. 2018; black) between 10 and 16 Nov 2018.

12 November resulted in deposition of nearly all CCN up to the peak 1% supersaturations being measured and a drop in CN > 10 nm concentrations to ~100 cm^{-3}. In contrast, 14–16 November rain-free days with ample solar insolation show growth of particles during the daytime from the Aitken to accumulation (CCN) mode. Opportunities exist to further study these new particle formation, growth, and wet-scavenging processes.

Clouds and precipitation. Clouds and precipitation were frequent over the AMF1 site with 191 of 212 days between 1 October and 30 April producing shallow liquid clouds, 165 of which had stratiform liquid clouds of greater than 30 min in duration over the site. Eighty-three days also produced deep convection over the site with 93 days producing gauge-measurable precipitation and 135 days producing disdrometer-measurable precipitation. Time–height object identification from vertically pointing radar and lidar data constituting the ARSCL (Active Remote Sensing of Cloud Locations) product (Clothiaux et al. 2001) show more than 3,400 shallow, liquid clouds were observed, with more than 650 lasting longer than 30 min. It also indicates over 2,700 primarily convective clouds with cloud bases > 0°C and tops < 0°C were observed with over 540 having cloud tops < –30°C (i.e., deep convective objects). Connecting these convective elements to one another via anvils yields over 1,100 separate convective systems, ~160 of which are deep convective systems (cloud tops < –30°C).

Low-level cloud cover increased significantly between the morning and late afternoon in association with orographic upslope flow (Fig. 12). Rainfall also exhibited a relative maximum in the late afternoon; however, overnight hours produced the greatest amount of rainfall and most frequent deep clouds (Fig. 12). This is consistent with the bimodal diurnal timing of deep convection initiation shown by Cancelada et al. (2020) and

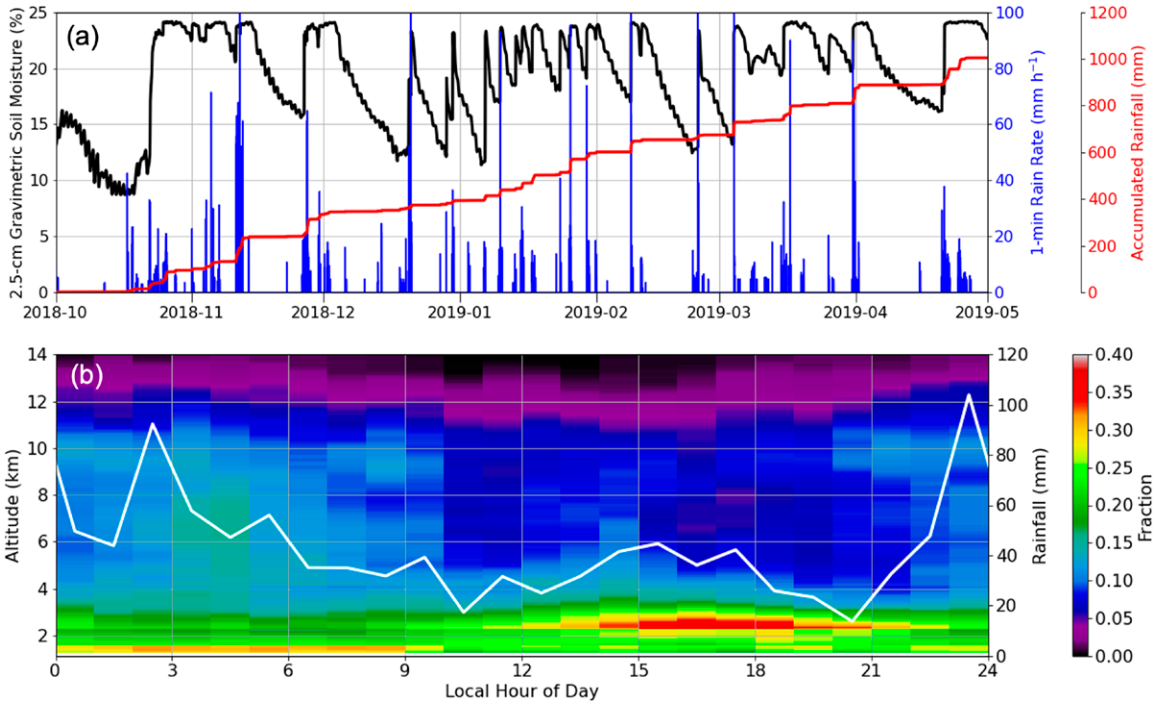

Fig. 12. (a) AMF1 Pluvio-2 1-min rain rate (blue) and accumulated rainfall (red) with soil moisture measurements (Sullivan et al. 2018) for the entire campaign. (b) Diurnal cycles of mean Ka-band ARM zenith radar (KAZR)-measured cloud and precipitation fraction by altitude from the ARSCL product (Fairless et al. 2018; color fill) and Pluvio-2 surface accumulated precipitation (white) between Oct 2018 and Apr 2019.

similar to parts of the U.S. Great Plains (Higgins et al. 1997; Wilson and Roberts 2006; Zhang and Klein 2010). Rainfall was spread throughout the campaign, accumulating to just over 1000 mm (Fig. 12). November, January, and March all produced 200 mm or more of rainfall with November (240 mm) having the most rainfall. December (60 mm) and February (just over 70 mm) were very suppressed in comparison. Much of this precipitation originated in heavy rainfall events frequently exceeding 50 mm with peak 1-min rain rates exceeding 100 mm h^{-1}, the greatest of which occurred on 11–12 November 2018 with just over 100 mm of rainfall (Fig. 11). Heavy rainfall events significantly increased soil moisture (Fig. 12), with potential impacts on surface fluxes and boundary layer evolution for the days that followed that require investigation.

Shallow convection. North–south–oriented orographic cumulus cloud lines aligned with the crest of the SDC formed on most days by afternoon hours. These cloud lines most frequently developed just east of the SDC crest but occasionally formed directly over the crest or along the western foothills depending on thermodynamic and kinematic profile of the lowest few kilometers of the troposphere. On days with strong inversions, several sampled by the G-1, these cumulus lines remained shallow but would commonly expand eastward into a stratocumulus layer by early evening. These widespread cloud layers were often detectable by the Ka-band radars and at times would begin drizzling, the causes of which are currently being investigated. An example is shown in Fig. 13, although liquid cloud drizzle onset cases vary significantly in their combinations of environmental and cloud properties.

Purely liquid raining clouds and drizzling fog (e.g., present as the early morning diurnal peak in Fig. 12) were also common on days with deeper precipitating clouds. These situations were often associated with stable, moist, and relatively clean low-level easterly upslope flow

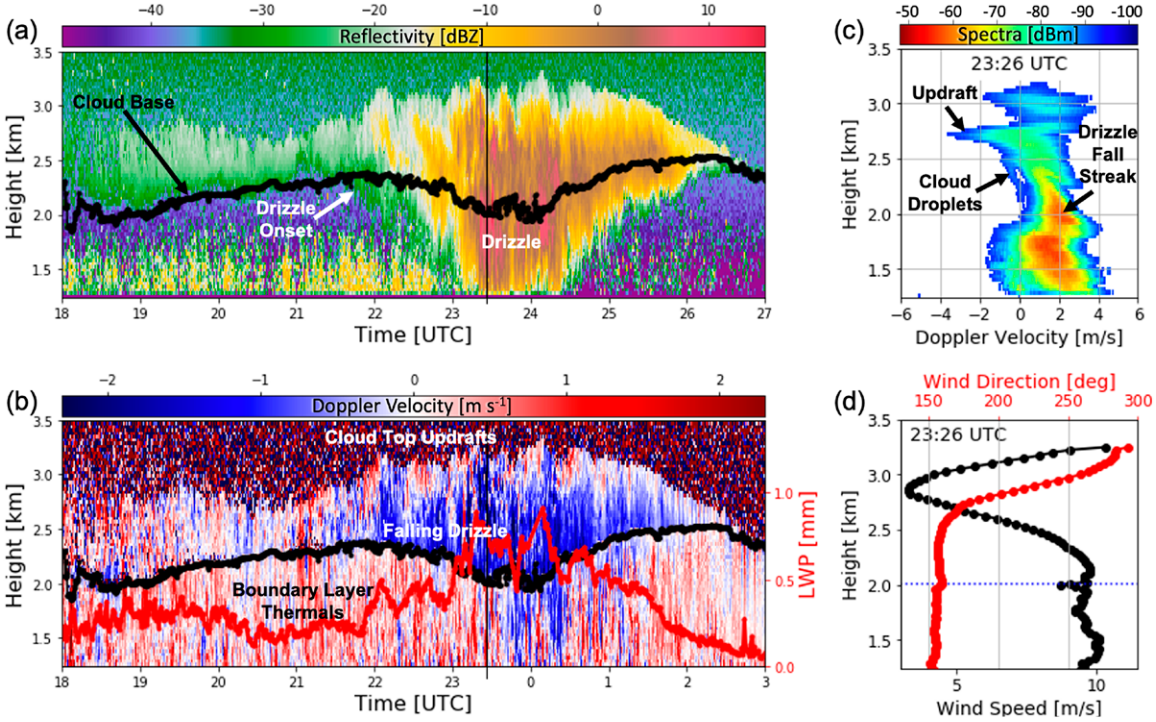

Fig. 13. An example stratocumulus event with drizzle onset. (left) 9-h time–height plots of (a) KAZR reflectivity (Johnson et al. 2018) and ceilometer (Morris and Ermold 2018) cloud base, and (b) combined KAZR and Doppler lidar (Newsom and Krishnamurthy 2018) mean Doppler velocity with microwave radiometer-retrieved liquid water path. (right) 2326 UTC vertical profiles of (c) KAZR Doppler spectra (Bharadwaj et al. 2018) and (d) combined Doppler lidar and Ka-SACR (Hardin et al. 2018c) velocity azimuth display horizontal wind retrievals (Kollias et al. 2014).

commonly produced by significant rainfall events. Precipitating convective clouds of moderate depth that likely contained ice were common, as were supercooled congestus clouds without ice reaching temperatures of –20°C or colder. The processes contributing to precipitation and ice formation in these clouds as they deepen and widen are a focus for future investigation. Several G-1 flights occurred during such events to examine near- and in-cloud conditions with one focus on the effects of detraining near stationary, orographic cloud lines on nearby free-tropospheric temperature and humidity that may reduce entrainment-driven buoyancy dilution in subsequent clouds following hypotheses summarized in Moser and Lasher-Trapp (2018).

Deep convection. Some orographic congestus initiated ice and precipitation with moderate to strong radar reflectivity values over periods of 30 min to several hours constituting successful deep convection initiation. Cells frequently initiated in multiple locations and interacted as time progressed. To track the evolution of cells including interactions through merging and splitting with neighboring cells, cells were identified using 15-min C-SAPR2 composite reflectivity and tracked using an updated version of FLEXTRKR (Feng et al. 2018, 2019). The mountainous terrain to the west of the site blocked PPI elevation angles up to 2°–5° depending on azimuth such that shallow cells west of the SDC are not detected; however, the deep mode is well captured by using composite rather than low-level reflectivity. For the ~3.5 months (1 October–26 December, 21 January–5 February, 22 February–2 March) that the C-SAPR2 collected PPI volumes, 6,895 cells were tracked with associated radar-retrieved properties. An example of identified cells and their tracks is shown in Fig. 14a with accumulated cell starting locations shown by density in Fig. 14b, highlighting the propensity for cells to form slightly east of the highest terrain and just west of the AMF1 site. Mean cell area increases moving eastward from the high terrain, indicative of upscale-growth events immediately east of the

high terrain (Fig. 14c). Current work involves matching radar HSRHI scans, AMF1-observed atmospheric conditions, and cell tracks to form a database for the study of factors influencing deep convective cloud life cycles.

Using the cell-track database and satellite-based MCS tracking, current research is focused on deep convection initiation and upscale growth processes. One focus is building on Nelson et al. (2021) to study how mesoscale and cloud-scale circulations couple with thermodynamic variability below and above cloud base to impact convective updraft properties critical to the formation of sustained precipitation. A second focus is understanding how cells evolve following sustained precipitation formation, particularly through convective downdrafts and cold pools that initiate new updrafts and may or may not promote upscale growth into MCSs. While many deep convective cells observed during CACTI grew upscale into supercells (e.g., Trapp et al. 2020) or mesoscale complexes, events during the IOP are of particular interest because of more extensive characterization via RELAMPAGO measurements. Extreme deep convective events are also a focus of investigation (e.g., Borque et al. 2020) including the 25 January 2019 event shown in Fig. 15 that produced a radar echo top near 21 km above sea level in a HSRHI scan with 40-dB*Z* echoes extending above 19 km.

Modeling. A number of modeling activities focused on CACTI cases are ongoing. A regional 3-km Weather Research and Forecasting simulation covering 15 October–30 April utilizing an aerosol-aware microphysics scheme (Thompson and Eidhammer 2014) was performed with output intended to match radar, satellite, and vertical profiling sampling frequencies to support direct model–observations comparisons (Zhang et al. 2021). Shallow orographic cloud occurrence, convection initiation, and upscale growth representation in this simulation are being evaluated, including sensitivities of convective cloud life cycles to model resolution since horizontal grid spacing > 500 m fails to fully resolve deep convective updrafts (Bryan et al. 2003; Bryan and Morrison 2012; Varble et al. 2020; Lebo and Morrison 2015; Verrelle et al. 2015). Future work will also investigate sensitivities to parameterized aerosol and microphysical processes with collected aerosol datasets available for model initialization.

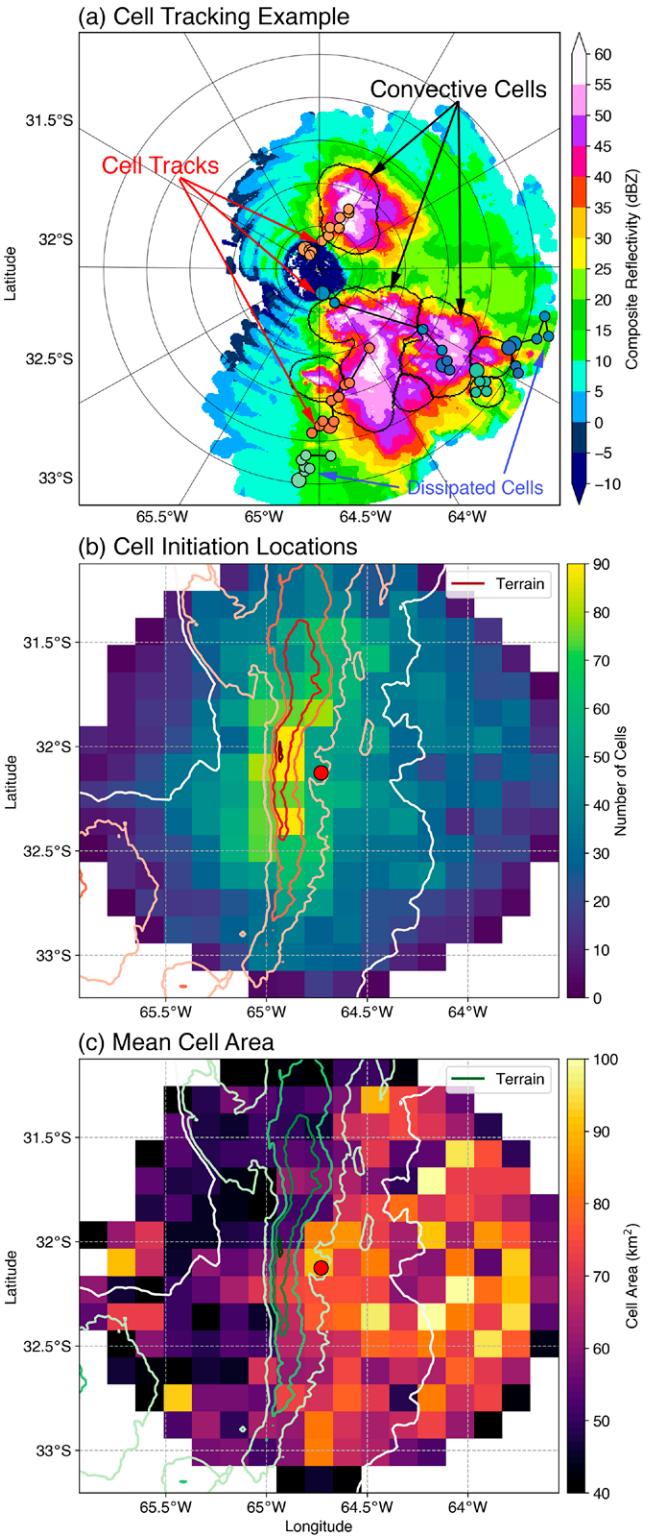

Fig. 14. (a) An example of C-SAPR2 identified convective cells outlined in black on composite reflectivity with individual cell tracks shown by connected colored symbols. (b) Cell starting locations by number. (c) The mean area of cells by location where terrain height is contoured every 500 m.

Large-eddy simulations better resolve convective updraft thermals, and ARM is expanding their LES ARM Symbiotic Simulation and Observation (LASSO) ensemble runs originally designed for shallow cumulus cases at the ARM SGP site (Gustafson et al. 2020) to handle CACTI orographic deep convection initiation events. These nested simulations with an inner mesoscale domain grid spacing of 100 m will be run in small ensembles for up to 10 cases or more to support convective cloud processes science, coarser model assessment, and parameterization evaluation with direct linkages to field campaign measurements. Output, as well as initialization and restart files, will be freely available to the research community.

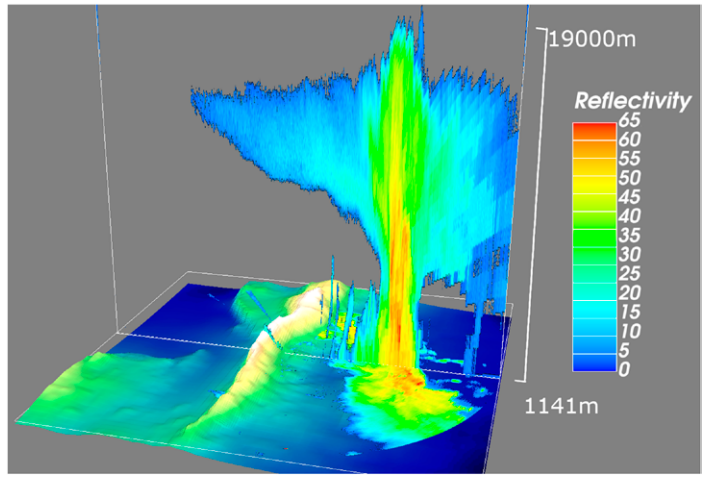

Fig. 15. A three-dimensional view toward the north-northwest of the SDC terrain colored by elevation with C-SAPR2 reflectivity observed by a HSRHI scan (Hardin et al. 2018a) and low-elevation PPI scan (Hardin et al. 2018b) slightly offset in time during the 25 Jan 2019 extreme deep convection event.

Summary and lessons learned

CACTI, together with RELAMPAGO, was the result of a large collaborative team of U.S. and Argentine scientists, facility and project managers, instrument engineers and technicians, dataset mentors, weather forecasters, and many more. Numerous challenges were encountered including delays in shipping, electrical grid dropouts, aircraft communications dropouts, and failure of C-band hardware components. The keys to overcoming these challenges were contingency planning, timely and effective communication, readiness to adjust measurement strategies, and individuals putting in extra time and effort. The success of this team resulted in a comprehensive collection of atmospheric state, aerosol, cloud, precipitation, radiation, and surface measurements at the surface and aloft, providing new opportunities to study atmospheric processes critical to weather and climate in a previously data-sparse region.

Several lessons can be gleaned from CACTI that may help future field campaigns be successful. First, the importance of site location cannot be overstated, so time and care should be put into site selection to best balance scientific needs with logistical limitations. This requires pre-campaign (at least 1–2 years ahead of time) research and planning with critical local support. Second, choosing appropriate sites and measurement strategies (e.g., when to launch radiosondes, how to scan a radar) also benefits greatly from pre-campaign data analysis. Third, consistent monitoring of data via near-real-time quick-look imagery is critical to identifying and fixing issues quickly to avoid degraded or missing data. Last, datasets with consistent measurement strategies (e.g., a regular radar scan sequence) are much easier to use and interpret than frequently changing strategies. However, there is also a need for innovative new techniques targeting critical phenomena (e.g., convective updrafts) that we still fail to adequately measure. Observing system simulation experiments provide a tool to formulate and test these techniques and should become standard for future major field campaigns to reduce subjectively chosen strategies.

The unique location of the experiment conducted over an entire warm season provides new opportunities for studying the life cycles of numerous convective clouds from initial cumulus formation through organization of deep convective systems within the context of thoroughly observed factors influencing their evolution. Shallow liquid clouds were observed directly overhead on 90% of the campaign days with ~160 deep convective systems and highly variable CCN and INP concentrations. Initial results show that deep convection initiation was most

frequent just east of the primary SDC ridgeline west of the AMF observing site with immediate deep convective upscale growth over and east of the AMF site. The rainfall diurnal cycle has a prominent nocturnal maximum with a secondary late afternoon peak. CIN minimizes in midafternoon followed by an early evening peak in CAPE and LNB that is similar to the mean diurnal peak of CN and CCN concentrations. These findings were generally expected but unquantified until now. Less expected were the high frequencies of elevated deep convection, drizzling fog and warm rain, aerosol growth and significant wet-scavenging events, and radar echo tops reaching nearly 21 km above sea level in the SDC foothills.

The first research studies from CACTI are just being published, and much of the research targeting processes in Fig. 1 is just beginning, from controls on warm rain and ice formation to determinants of updraft size, shape, strength including entrainment and detrainment, and from the formation of downdrafts and their role in cold pools and deep convective upscale growth to interactions of aerosol and cloud life cycles with one another and with complex terrain affected circulations. Such studies combined with high-resolution modeling will improve process-level understanding but also be critical for evaluating and improving aerosol and cloud process parameterizations in next-generation weather and climate models.

Acknowledgments. We thank the U.S. DOE ARM program for funding CACTI and many other agencies and individuals for their invaluable support including ARM managers, engineers, technicians, instrument and data mentors, the ARM Data Center, and other support staff. We thank the following individuals for their significant contributions to CACTI: Kim Nitschke, Juarez Viegas, Bruno Cunha, Tercio Silva, Kaitlyn Suski, Stephen Springston, Art Sedlacek, Mike Hubbell, Dan Nelson, Mike Crocker, Pete Carroll, Matt Newburn, Albert Mendoza, Clayton Eveland, Jon Ray, Jennifer Armstrong, Andrei Lindenmaier, Pete Argay, Todd Houchins, Brad Isom, Jennifer Comstock, Hanna Goss, Conrado Javier Rodriguez, Emilia Ludueña, Julio Bourdin, Mariano Palermo, Gustavo Cabrera, and Martin Rugna. Several individuals including Eldo Avila, David Gochis, Robert Houze, Jr., Michael Jensen, Pavlos Kollias, L. Ruby Leung, Kristen Rasmussen, and Christopher Williams contributed to pre-campaign planning. We thank RELAMPAGO PIs, graduate students, and support provided by NSF and NCAR EOL. We greatly appreciate INVAP S.E. for providing in-country project management. We are grateful to SMN for major in-country support, launching radiosondes and providing forecasting support. Siting and import/export of instrumentation was critically facilitated by AMF1 site landowner Eduardo Castro, the Villa Yacanto city council, Hamelmann Communications, the Córdoba provincial government (Ministry of Science and Technology; Ministry of Water, Environment and Public Services), the national government of Argentina (Ministry of Science, Technology, and Innovation; Ministry of Foreign Affairs, International Trade, and Worship), the U.S. Embassy in Argentina, Fuerza Aérea Argentina, Administración Nacional de Aviación Civil, and Aeropuertos Argentina 2000. Forecasting was additionally supported by the University of Buenos Aires, University of Illinois, CSU and University of Washington. Computing support was provided by the Compute and Data Environment for Science at Oak Ridge National Laboratory, National Energy Research Scientific Computing Center at Lawrence Berkeley National Laboratory, the University of Utah Center for High Performance Computing, and the Computational and Information Systems Laboratory at NCAR. Funding was provided by the U.S. DOE Office of Science Biological and Environmental Research as part of the Atmospheric System Research program and NSF Grants AGS-1661662, AGS-1661799, and AGS-1661707. Pacific Northwest National Laboratory is operated by Battelle for the U.S. DOE under Contract DE-AC05-76RLO1830. Last, we thank three anonymous reviewers for helpful comments.

Data availability statement. All CACTI data are available through links provided at www.arm.gov/research/campaigns/amf2018cacti.

References

Anabor, V., D. J. Stensrud, and O. L. L. de Moraes, 2008: Serial upstream-propagating mesoscale convective system events over southeastern South America. *Mon. Wea. Rev.*, **136**, 3087–3105, https://doi.org/10.1175/2007MWR2334.1.

Anderson, C. J., and Coauthors, 2003: Hydrological processes in regional climate model simulations of the central United States flood of June–July 1993. *J. Hydrometeor.*, **4**, 584–598, https://doi.org/10.1175/1525-7541(2003)004<0584:HPIRCM>2.0.CO;2.

Bechis, H., P. Salio, and J. J. Ruiz, 2020: Drylines in Argentina: Synoptic climatology and processes leading to their genesis. *Mon. Wea. Rev.*, **148**, 111–129, https://doi.org/10.1175/MWR-D-19-0050.1.

Bedka, K. M., and K. Khlopenkov, 2016: A probabilistic multispectral pattern recognition method for detection of overshooting cloud tops using passive satellite imager observations. *J. Appl. Meteor. Climatol.*, **55**, 1983–2005, https://doi.org/10.1175/JAMC-D-15-0249.1.

Bharadwaj, N., J. Hardin, B. Isom, A. Lindenmaier, A. Matthews, and D. Nelson, 2018: Ka-band ARM zenith radar filtered spectral data: General co-polarized mode (KAZRSPECCMASKGECOPOL). ARM User Facility, accessed 15 May 2020, https://doi.org/10.5439/1025218.

Borque, P., P. Salio, M. Nicolini, and Y. G. Skabar, 2010: Environment associated with deep moist convection under SALLJ conditions: A case study. *Wea. Forecasting*, **25**, 970–984, https://doi.org/10.1175/2010WAF2222352.1.

——, E. P. Luke, P. Kollias, and F. Yang, 2018: Relationship between turbulence and drizzle in continental and marine low stratiform clouds. *J. Atmos. Sci.*, **75**, 4139–4148, https://doi.org/10.1175/JAS-D-18-0060.1.

——, L. Vidal, M. Rugna, T. J. Lang, M. G. Nicora, and S. W. Nesbitt, 2020: Distinctive signals in 1-minute observations of overshooting tops and lightning activity in a severe supercell thunderstorm. *J. Geophys. Res. Atmos.*, **125**, e2020JD032856, https://doi.org/10.1029/2020JD032856.

Bryan, G. H., and H. Morrison, 2012: Sensitivity of a simulated squall line to horizontal resolution and parameterization of microphysics. *Mon. Wea. Rev.*, **140**, 202–225, https://doi.org/10.1175/MWR-D-11-00046.1.

——, J. C. Wyngaard, and J. M. Fritsch, 2003: Resolution requirements for the simulation of deep moist convection. *Mon. Wea. Rev.*, **131**, 2394–2416, https://doi.org/10.1175/1520-0493(2003)131<2394:RRFTSO>2.0.CO;2.

Bueno Repinaldo, H. F., M. Nicolini, and Y. G. Skabar, 2015: Characterizing the diurnal cycle of low-level circulation and convergence using CFSR data in southeastern South America. *J. Appl. Meteor. Climatol.*, **54**, 671–690, https://doi.org/10.1175/JAMC-D-14-0114.1.

Camponogara, G., M. A. F. Silva Dias, and G. G. Carrio, 2014: Relationship between Amazon biomass burning aerosols and rainfall over the La Plata basin. *Atmos. Chem. Phys.*, **14**, 4397–4407, https://doi.org/10.5194/acp-14-4397-2014.

Cancelada, M., P. Salio, and S. W. Nesbitt, 2019: CCN source regions during RELAMPAGO-CACTI field campaign. *2019 Fall Meeting*, San Francisco, CA, Amer. Geophys. Union, Abstract A53U-3048, https://doi.org/10.1002/essoar.10506532.1.

——, ——, D. Vila, S. W. Nesbitt, and L. Vidal, 2020: Backward adaptive brightness temperature threshold technique (BAB3T): A methodology to determine extreme convective initiation regions using satellite infrared imagery. *Remote Sens.*, **12**, 337, https://doi.org/10.3390/rs12020337.

Carril, A. F., and Coauthors, 2012: Performance of a multi-RCM ensemble for south eastern South America. *Climate Dyn.*, **39**, 2747–2768, https://doi.org/10.1007/s00382-012-1573-z.

Cecil, D. J., and C. B. Blankenship, 2012: Toward a global climatology of severe hailstorms as estimated by satellite passive microwave imagers. *J. Climate*, **25**, 687–703, https://doi.org/10.1175/JCLI-D-11-00130.1.

——, D. E. Buechler, and R. J. Blakeslee, 2015: TRMM LIS climatology of thunderstorm occurrence and conditional lightning flash rates. *J. Climate*, **28**, 6536–6547, https://doi.org/10.1175/JCLI-D-15-0124.1.

Clothiaux, E. E., and Coauthors, 2001: The ARM millimeter wave cloud radars (MMCRs) and the active remote sensing of clouds (ARSCL) value added product (VAP). DOE Tech. Memo. ARMVAP-002.1, 56 pp., www.arm.gov/publications/tech_reports/arm-vap-002-1.pdf.

Dai, A., 2006: Precipitation characteristics in eighteen coupled climate models. *J. Climate*, **19**, 4605–4630, https://doi.org/10.1175/JCLI3884.1.

Damiani, R., and Coauthors, 2008: The Cumulus, Photogrammetric, In Situ, and Doppler Observations Experiment of 2006. *Bull. Amer. Meteor. Soc.*, **89**, 57–74, https://doi.org/10.1175/BAMS-89-1-57.

Del Genio, A. D., J. Wu, and Y. Chen, 2012: Characteristics of mesoscale organization in WRF simulations of convection during TWP-ICE. *J. Climate*, **25**, 5666–5688, https://doi.org/10.1175/JCLI-D-11-00422.1.

Della Ceca, L. S., M. F. G. Ferreyra, A. Lyapustin, A. Chudnovsky, L. Otero, H. Carreras, and F. Barnaba, 2018: Satellite-based view of the aerosol spatial and temporal variability in the Córdoba region (Argentina) using over ten years of high-resolution data. *ISPRS J. Photogramm. Remote Sens.*, **145**, 250–267, https://doi.org/10.1016/j.isprsjprs.2018.08.016.

DeMott, P. J., and T. C. J. Hill, 2020a: Cloud, Aerosol, and Complex Terrain Interactions (CACTI) ARM Mobile Facility (AMF) Measurements of Ice Nucleating Particles Field Campaign Report. Tech. Doc. DOE/SC-ARM-20-006, 8 pp., www.arm.gov/publications/programdocs/doe-sc-arm-20-006.pdf.

——, and ——, 2020b: Cloud, Aerosol, and Complex Terrain Interactions (CACTI) ARM Aerial Facility (AAF) Measurements of Ice Nucleating Particles Field Campaign Report. Tech. Doc. DOE/SC-ARM-20-008, 9 pp., www.arm.gov/publications/programdocs/doe-sc-arm-20-008.pdf.

DeMott, P. J., and ——, 2020c: CACTI ARM Aerial Facility Measurements of Ice Nucleating Particles. ARM User Facility, accessed 25 August 2021, https://doi.org/10.5439/1607793.

DeMott, P. J., and ——, 2020d: CACTI ARM Mobile Facility Measurements of Ice Nucleating Particles. ARM User Facility, accessed 25 August 2021, https://doi.org/10.5439/1607786.

——, ——, and G. McFarquhar, 2018a: Measurements of Aerosols, Radiation, and Clouds over the Southern Ocean (MARCUS) Ice Nucleating Particle Measurements Field Campaign Report. Tech. Doc. DOE/SC-ARM-18-031, 6 pp., www.arm.gov/publications/programdocs/doe-sc-arm-18-031.pdf.

——, and Coauthors, 2018b: The Fifth International Workshop on Ice Nucleation phase 2 (FIN-02): Laboratory intercomparison of ice nucleation measurements. *Atmos. Meas. Tech.*, **11**, 6231–6257, https://doi.org/10.5194/amt-11-6231-2018.

Durkee, J. D., and T. L. Mote, 2009: A climatology of warm-season mesoscale convective complexes in subtropical South America. *Int. J. Climatol.*, **30**, 418–431, https://doi.org/10.1002/joc.1893.

——, ——, and J. M. Shepherd, 2009: The contribution of mesoscale convective complexes to rainfall across subtropical South America. *J. Climate*, **22**, 4590–4605, https://doi.org/10.1175/2009JCLI2858.1.

Fairless, T., and S. Giangrande, 2018: Interpolated Sonde (INTERPOLATEDSONDE). ARM User Facility, accessed 16 July 2019, https://doi.org/10.5439/1095316.

——, ——, K. Johnson, E. Clothiaux, and P. Kollias, 2018: Active Remote Sensing of CLouds (ARSCL) product using Ka-band ARM zenith radars (ARSCLKAZR1KOLLIAS). ARM User Facility, accessed 17 September 2020, https://doi.org/10.5439/1350629.

Fan, J., and Coauthors, 2017: Cloud-resolving model intercomparison of an MC3E squall line case: Part I – Convective updrafts. *J. Geophys. Res.*, **122**, 9351–9378, https://doi.org/10.1002/2017JD026622.

——, and Coauthors, 2019: Overview of the HI-SCALE field campaign: A new perspective on shallow convective clouds. *Bull. Amer. Meteor. Soc.*, **100**, 821–840, https://doi.org/10.1175/BAMS-D-18-0030.1.

Feng, Z., and Coauthors, 2018: Structure and evolution of mesoscale convective systems: Sensitivity to cloud microphysics in convection-permitting simulations over the United States. *J. Adv. Model. Earth Syst.*, **10**, 1470–1494, https://doi.org/10.1029/2018MS001305.

——, and Coauthors, 2019: Spatiotemporal characteristics and large-scale environments of mesoscale convective systems east of the Rocky Mountains. *J. Climate*, **32**, 7303–7328, https://doi.org/10.1175/JCLI-D-19-0137.1.

Freitas, S. R., and Coauthors, 2005: Monitoring the transport of biomass-burning emissions in South America. *Environ. Fluid Mech.*, **5**, 135–167, https://doi.org/10.1007/s10652-005-0243-7.

Fridlind, A. M., and Coauthors, 2012: A comparison of TWP-ICE observational data with cloud-resolving model results. *J. Geophys. Res.*, **117**, D05204, https://doi.org/10.1029/2011JD016595.

Gustafson, W. I., and Coauthors, 2020: The Large-Eddy Simulation (LES) Atmospheric Radiation Measurement (ARM) Symbiotic Simulation and Observation (LASSO) activity for continental shallow convection. *Bull. Amer. Meteor. Soc.*, **101**, E462–E479, https://doi.org/10.1175/BAMS-D-19-0065.1.

Hagos, S., Z. Feng, C. D. Burleyson, K.-S. S. Lim, C. N. Long, D. Wu, and G. Thompson, 2014: Evaluation of convection-permitting model simulations of cloud populations associated with the Madden-Julian Oscillation using data collected during the AMIE/DYNAMO field campaign. *J. Geophys. Res. Atmos.*, **119**, 122052–122068, https://doi.org/10.1002/2014JD022143.

Han, B., and Coauthors, 2019: Cloud-resolving model intercomparison of an MC3E squall line case: Part II. Stratiform precipitation properties. *J. Geophys. Res. Atmos.*, **124**, 1090–1117, https://doi.org/10.1029/2018JD029596.

Hardin, J., A. Hunzinger, E. Schuman, A. Matthews, N. Bharadwaj, A. Varble, K. Johnson, and S. Giangrande, 2018a: C-band Scanning ARM Precipitation Radar, CF-Radial, Quality-Controlled Hemispheric Range-Height Indicator Scans (CSAPR2CFRHSRHIQC). ARM User Facility, accessed 1 October 2020, https://doi.org/10.5439/1615607.

——, ——, ——, ——, ——, ——, ——, and ——, 2018b: C-band Scanning ARM Precipitation Radar, CF-Radial, Quality-Controlled Plan-Position Indicator Scans (CSAPR2CFRPPIQC). ARM User Facility, accessed 1 October 2020, https://doi.org/10.5439/1615604.

——, ——, ——, ——, ——, ——, ——, and ——, 2018c: Ka-Band Scanning ARM Cloud Radar, CF-Radial, Quality-Controlled Hemispheric Range-Height Indicator Scans (KASACRCFRHSRHIQC). ARM User Facility, accessed 14 May 2020, https://doi.org/10.5439/1615605.

——, ——, ——, ——, ——, ——, ——, and ——, 2020: CACTI Radar b1 Processing: Corrections, Calibrations, and Processing Report. Tech. Doc. DOE/SC-ARM-TR-244, 46 pp., https://arm.gov/publications/brochures/doe-sc-arm-tr-244.pdf.

Higgins, R. W., Y. Yao, E. S. Yarosh, J. E. Janowiak, and K. C. Mo, 1997: Influence of the great plains low-level jet on summertime precipitation and moisture transport over the central United States. *J. Climate*, **10**, 481–507, https://doi.org/10.1175/1520-0442(1997)010<0481:IOTGPL>2.0.CO;2.

Hill, T. C. J., P. J. DeMott, Y. Tobo, J. Fröhlich-Nowoisky, B. F. Moffett, G. D. Franc, and S. M. Kreidenweis, 2016: Sources of organic ice nucleating particles in soils. *Atmos. Chem. Phys.*, **16**, 7195–7211, https://doi.org/10.5194/acp-16-7195-2016.

——, ——, F. Conen, and O. Möhler, 2018: Impacts of bioaerosols on atmospheric ice nucleation processes. *Microbiology of Aerosols*, 1st ed. A.-M. Delort and P. Amato, Eds., John Wiley & Sons, 155–194, https://doi.org/10.1002/9781119132318.ch3a.

Hohenegger, C., and B. Stevens, 2013: Preconditioning deep convection with cumulus congestus. *J. Atmos. Sci.*, **70**, 448–464, https://doi.org/10.1175/JAS-D-12-089.1.

Holdridge, D., E. Keeler, and J. Kyrouac, 2018: Balloon-Borne Sounding System (SONDEWNPN). ARM User Facility, accessed 26 July 2019, https://doi.org/10.5439/1021460.

Houze, R. A., 2012: Orographic effects on precipitating clouds. *Rev. Geophys.*, **50**, RG1001, https://doi.org/10.1029/2011RG000365.

Hunzinger, A., J. C. Hardin, N. Bharadwaj, A. Varble, and A. Matthews, 2020: An extended radar relative calibration adjustment (eRCA) technique for higher-frequency radars and range–height indicator (RHI) scans. *Atmos. Meas. Tech.*, **13**, 3147–3166, https://doi.org/10.5194/amt-13-3147-2020.

Johnson, K., T. Fairless, and S. Giangrande, 2018: Ka-Band ARM zenith radar (KAZR) CF-Radial, Corrected VAP, General Mode (KAZRCFRCORGE). ARM User Facility, accessed 14 May 2020, https://doi.org/10.5439/1642217.

Klein, C., and C. M. Taylor, C., 2020: Dry soils can intensify mesoscale convective systems. *Proc. Natl. Acad. Sci. USA*, **117**, 21 132–21 137, https://doi.org/10.1073/pnas.2007998117.

Klein, S. A., X. Jiang, J. Boyle, S. Malyshev, and S. Xie, 2006: Diagnosis of the summertime warm and dry bias over the U.S. Southern Great Plains in the GFDL climate model using a weather forecasting approach. *Geophys. Res. Lett.*, **33**, L18805, https://doi.org/10.1029/2006GL027567.

Kollias, P., and Coauthors, 2014: Scanning ARM Cloud Radars. Part II: Data quality control and processing. *J. Atmos. Oceanic Technol.*, **31**, 583–598, https://doi.org/10.1175/JTECH-D-13-00045.1.

Kuang, C., S. Salwen, M. Boyer, and A. Singh, 2018a: Condensation Particle Counter (AOSCPCF). ARM User Facility, accessed 23 December 2019, https://doi.org/10.5439/1046184.

——, ——, ——, and ——, 2018b: Scanning Mobility Particle Sizer (AOSSMPS). ARM User Facility, accessed 23 December 2019, https://doi.org/10.5439/1095583.

Kumjian, M. R., and Coauthors, 2020: Gargantuan hail in Argentina. *Bull. Amer. Meteor. Soc.*, **101**, E1241–E1258, https://doi.org/10.1175/BAMS-D-19-0012.1.

Laing, A. G., and J. M. Fritsch, 1997: The global population of mesoscale convective complexes. *Quart. J. Roy. Meteor. Soc.*, **123**, 389–405, https://doi.org/10.1002/qj.49712353807.

Lang, S. E., W. Tao, X. Zeng, and Y. Li, 2011: Reducing the biases in simulated radar reflectivities from a bulk microphysics scheme: Tropical convective systems. *J. Atmos. Sci.*, **68**, 2306–2320, https://doi.org/10.1175/JAS-D-10-05000.1.

Lebo, Z. J., and H. Morrison, 2015: Effects of horizontal and vertical grid spacing on mixing in simulated squall lines and implications for convective strength and structure. *Mon. Wea. Rev.*, **143**, 4355–4375, https://doi.org/10.1175/MWR-D-15-0154.1.

Levin, E. J. T., and Coauthors, 2019: Characteristics of ice nucleating particles in and around California winter storms. *J. Geophys. Res.*, **124**, 11 530–11 551, https://doi.org/10.1029/2019JD030831.

Marinescu, P. J., S. C. van den Heever, S. M. Saleeby, and S. M. Kreidenweis, 2016: The microphysical contributions to and evolution of latent heating profiles in two MC3E MCSs. *J. Geophys. Res. Atmos.*, **121**, 7913–7935, https://doi.org/10.1002/2016JD024762.

Marquis, J. N., A. C. Varble, P. Robinson, T. C. Nelson, and K. Friedrich, 2021: Low-level mesoscale and cloud-scale interactions promoting deep convective initiation. *Mon. Wea. Rev.*, **8**, 2473–2495, https://doi.org/10.1175/MWR-D-20-0391.1.

Mather, J. H., and J. W. Voyles, 2013: The ARM Climate Research Facility: A review of structure and capabilities. *Bull. Amer. Meteor. Soc.*, **94**, 377–392, https://doi.org/10.1175/BAMS-D-11-00218.1.

Matthews, A., and D. Nelson, 2018: Water Content Meter aboard aircraft (AAFWCM). ARM User Facility, accessed 26 October 2020, https://doi.org/10.5439/1632815.

Mei, F., and M. Pekour, 2018a: Cloud Condensation Nuclei Particle Counter aboard aircraft (AAFCCN2COLA). ARM User Facility, accessed 26 October 2020, https://doi.org/10.5439/1482582.

Mei, F., and M. Pekour, 2018b: Condensation Particle Counter aboard aircraft (AAFCPCFISO). ARM User Facility, accessed 26 October 2020, https://doi.org/10.5439/1368538.

——, D. Zhang, and D. Nelson, 2018: Fast Cloud Droplet Probe aboard aircraft (AAFFCDP). ARM User Facility, accessed 26 October 2020, https://doi.org/10.5439/1417472.

Morris, V., and B. Ermold, 2018: Ceilometer (CEIL). ARM User Facility, accessed 14 May 2020, https://doi.org/10.5439/1181954.

Moser, D. H., and S. Lasher-Trapp, 2018: Cloud-spacing effects upon entrainment and rainfall along a convective line. *J. Appl. Meteor. Climatol.*, **57**, 1865–1882, https://doi.org/10.1175/JAMC-D-17-0363.1.

Mulholland, J. P., S. W. Nesbitt, R. J. Trapp, K. L. Rasmussen, and P. V. Salio, 2018: Convective storm life cycle and environments near the Sierras de Córdoba, Argentina. *Mon. Wea. Rev.*, **146**, 2541–2557, https://doi.org/10.1175/MWR-D-18-0081.1.

——, ——, and ——, 2019: A case study of terrain influences on upscale convective growth of a supercell. *Mon. Wea. Rev.*, **147**, 4305–4324, https://doi.org/10.1175/MWR-D-19-0099.1.

——, ——, ——, and J. M. Peters, 2020: The influence of terrain on the convective environment and associated convective morphology from an idealized modeling prospective. *J. Atmos. Sci.*, **77**, 3929–3949, https://doi.org/10.1175/JAS-D-19-0190.1.

Nelson, T. C., J. Marquis, A. Varble, and K. Friedrich, 2021: Radiosonde observations of environments supporting deep moist convection initiation during RELAMPAGO-CACTI. *Mon. Wea. Rev.*, **149**, 289–309, https://doi.org/10.1175/MWR-D-20-0148.1.

Nesbitt, S. W., R. Cifelli, and S. A. Rutledge, 2006: Storm morphology and rainfall characteristics of TRMM precipitation features. *Mon. Wea. Rev.*, **134**, 2702–2721, https://doi.org/10.1175/MWR3200.1.

——, and Coauthors, 2021: A storm safari in subtropical South America: Proyecto RELAMPAGO. **102**, E1621–E1644, *Bull. Amer. Meteor. Soc*., https://doi.org/10.1175/BAMS-D-20-0029.1.

Newsom, R., and R. Krishnamurthy, 2018: Doppler Lidar (DLFPT). ARM User Facility, accessed 14 May 2020, https://doi.org/10.5439/1025185.

Nicolini, M., and Y. G. Skabar, 2011: Diurnal cycle in convergence patterns in the boundary layer east of the Andes and convection. *Atmos. Res.*, **100**, 377–390, https://doi.org/10.1016/j.atmosres.2010.09.019.

——, C. Saulo, J. C. Torres, and P. Salio, 2002: Strong South American low level jet events characterization during warm season and implications for enhanced precipitation. *Meteorologica*, **27**, 59–69.

Öktem, R. J., and D. Romps, 2021: Point Cloud of Cloud Points (PCCP). ARM User Facility, accessed 1 October 2020, https://doi.org/10.5439/18048912.

——, Prabhat, J. Lee, A. Thomas, P. Zuidemaand, and D. M. Romps, 2014: Stereophotogrammetry of oceanic clouds. *J. Atmos. Oceanic Technol.*, **31**, 1482–1501, https://doi.org/10.1175/JTECH-D-13-00224.1.

O'Sullivan, D., and Coauthors, 2018: Contributions of biogenic material to the atmospheric ice-nucleating particle population in north western Europe. *Sci. Rep.*, **8**, 13 821, https://doi.org/10.1038/s41598-018-31981-7.

Qian, Y., and Coauthors, 2020: Neglecting irrigation contributes to the simulated summertime warm-and-dry bias in the central United States. *NPJ Climate Atmos. Sci.*, **3**, 31, https://doi.org/10.1038/s41612-020-00135-w.

Rasmussen, K. L., and R. A. Houze Jr., 2011: Orogenic convection in South America as seen by the TRMM satellite. *Mon. Wea. Rev.*, **139**, 2399–2420, https://doi.org/10.1175/MWR-D-10-05006.1.

——, and ——, 2016: Convective initiation near the Andes in subtropical South America. *Mon. Wea. Rev.*, **144**, 2351–2374, https://doi.org/10.1175/MWR-D-15-0058.1.

——, M. D. Zuluaga, and R. A. Houze Jr., 2014: Severe convection and lightning in subtropical South America. *Geophys. Res. Lett.*, **41**, 7359–7366, https://doi.org/10.1002/2014GL061767.

——, M. M. Chaplin, M. D. Zuluaga, and R. A. Houze Jr., 2016: Contribution of extreme convective storms to rainfall in South America. *J. Hydrometeor.*, **17**, 353–367, https://doi.org/10.1175/JHM-D-15-0067.1.

Ribeiro, B. Z., and L. F. Bosart, 2018: Elevated mixed layers and associated severe thunderstorm environments in South and North America. *Mon. Wea. Rev.*, **146**, 3–28, https://doi.org/10.1175/MWR-D-17-0121.1.

Romatschke, U., and R. A. Houze Jr., 2010: Extreme summer convection in South America. *J. Climate*, **23**, 3761–3791, https://doi.org/10.1175/2010JCLI3465.1.

Ruscica, R. C., A. A. Sörensson, and C. G. Menéndez, 2015: Pathways between soil moisture and precipitation in southeastern South America. *Atmos. Sci. Lett.*, **16**, 267–272, https://doi.org/10.1002/asl2.552.

Salio, P., M. Nicolini, and A. C. Saulo, 2002: Chaco low level jet events characterization during the austral summer season by ERA reanalysis. *J. Geophys. Res.*, **107**, 4816, https://doi.org/10.1029/2001JD001315.

——, ——, and E. J. Zipser, 2007: Mesoscale convective systems over southeastern South America and their relationship with the South American low-level jet. *Mon. Wea. Rev.*, **135**, 1290–1309, https://doi.org/10.1175/MWR3305.1.

Saulo, A. C., M. E. Seluchi, and M. Nicolini, 2004: A case study of a Chaco low-level jet event. *Mon. Wea. Rev.*, **132**, 2669–2683, https://doi.org/10.1175/MWR2815.1.

——, J. Ruiz, and Y. G. Skabar, 2007: Synergism between the low-level jet and organized convection at its exit region. *Mon. Wea. Rev.*, **135**, 1310–1326, https://doi.org/10.1175/MWR3317.1.

——, L. Ferreira, J. Nogués-Paegle, M. Seluchi, and J. Ruiz, 2010: Land–atmosphere interactions during a northwestern Argentina low event. *Mon. Wea. Rev.*, **138**, 2481–2498, https://doi.org/10.1175/2010MWR3227.1.

Schmid, B., and Coauthors, 2014: The DOE ARM Aerial Facility. *Bull. Amer. Meteor. Soc.*, **95**, 723–742, https://doi.org/10.1175/BAMS-D-13-00040.1.

Schumacher, R. S., and Coauthors, 2021: Convective-storm environments in subtropical South America from high-frequency soundings during RELAMPAGO-CACTI. *Mon. Wea. Rev.*, **149**, 1439–1458, https://doi.org/10.1175/MWR-D-20-0293.1.

Seluchi, M. E., A. C. Saulo, M. Nicolini, and P. Satyamurty, 2003: The Northwestern Argentinean low: A study of two typical events. *Mon. Wea. Rev.*, **131**, 2361–2378, https://doi.org/10.1175/1520-0493(2003)131<2361:TNALAS>2.0.CO;2.

——, R. Garreaud, F. A. Norte, and A. C. Saulo, 2006: Influence of the subtropical Andes on baroclinic disturbances: A cold front case study. *Mon. Wea. Rev.*, **134**, 3317–3335, https://doi.org/10.1175/MWR3247.1.

Smith, R. B., and Coauthors, 2012: Orographic precipitation in the tropics: The Dominica Experiment. *Bull. Amer. Meteor. Soc.*, **93**, 1567–1579, https://doi.org/10.1175/BAMS-D-11-00194.1.

Solman, S. A., and Coauthors, 2013: Evaluation of an ensemble regional climate model simulations over South America driven by the ERA-Interim reanalyses: Model performance and uncertainties. *Climate Dyn.*, **41**, 1139–1157, https://doi.org/10.1007/s00382-013-1667-2.

Song, H., W. Lin, Y. Lin, A. B. Wolf, R. Neggers, L. J. Donner, A. D. Del Genio, and Y. Liu, 2013: Evaluation of precipitation simulated by seven SCMs against the ARM observations at the SGP site. *J. Climate*, **26**, 5467–5492, https://doi.org/10.1175/JCLI-D-12-00263.1.

Sörensson, A. A., and C. G. Menéndez, 2011: Soil-precipitation coupling in South America. *Tellus*, **63A**, 56–68, https://doi.org/10.1111/j.1600-0870.2010.00468.x.

Stanford, M. W., A. Varble, E. Zipser, J. W. Strapp, D. Leroy, A. Schwarzenboeck, R. Potts, and A. Protat, 2017: A ubiquitous ice size bias in simulations of tropical deep convection. *Atmos. Chem. Phys.*, **17**, 9599–9621, https://doi.org/10.5194/acp-17-9599-2017.

Sullivan, R., D. Cook, and E. Keeler, 2018: Surface Energy Balance System (SEBS). ARM User Facility, accessed 10 August 2020, https://doi.org/10.5439/1025274.

Suski, K. J., T. C. J. Hill, E. J. T. Levin, A. Miller, P. J. DeMott, and S. M. Kreidenweis, 2018: Agricultural harvesting emissions of ice-nucleating particles. *Atmos. Chem. Phys.*, **18**, 13 755–13 771, https://doi.org/10.5194/acp-18-13755-2018.

Taylor, C. M., R. A. M. de Jeu, F. Guichard, P. P. Harris, and W. A. Dorigo, 2012: Afternoon rain more likely over drier soils. *Nature*, **489**, 423–426, https://doi.org/10.1038/nature11377.

Thompson, G., and T. Eidhammer, 2014: A study of aerosol impacts on clouds and precipitation development in a large winter cyclone. *J. Atmos. Sci.*, **71**, 3636–3658, https://doi.org/10.1175/JAS-D-13-0305.1.

Trapp, R. J., and Coauthors, 2020: Multiple-platform and multiple-Doppler radar observations of a supercell thunderstorm in South America during RELAMPAGO. *Mon. Wea. Rev.*, **148**, 3225–3241, https://doi.org/10.1175/MWR-D-20-0125.1.

Uin, J., C. Salwen, and G. Senum, 2018: Cloud Condensation Nuclei Particle Counter (AOSCCN2COLAAVG). ARM User Facility, accessed 23 December 2019.

Varble, A., 2018: Erroneous attribution of deep convective invigoration to aerosol concentration. *J. Atmos. Sci.*, **75**, 1351–1368, https://doi.org/10.1175/JAS-D-17-0217.1.

——, and Coauthors, 2011: Evaluation of cloud-resolving model intercomparison simulations using TWP-ICE observations: Precipitation and cloud structure. *J. Geophys. Res.*, **116**, D12206, https://doi.org/10.1029/2010JD015180.

——, and Coauthors, 2014a: Evaluation of cloud-resolving and limited area model intercomparison simulations using TWP-ICE observations: 1. Deep

convective updraft properties. *J. Geophys. Res. Atmos.*, **119**, 13 891–13 918, https://doi.org/10.1002/2013JD021371.

——, and Coauthors, 2014b: Evaluation of cloud-resolving and limited area model intercomparison simulations using TWP-ICE observations: 2. Precipitation microphysics. *J. Geophys. Res. Atmos.*, **119**, 13 919–13 945, https://doi.org/10.1002/2013JD021372.

——, and Coauthors, 2019: Cloud, Aerosol, and Complex Terrain Interactions (CACTI) Field Campaign Report. Tech. Doc. DOE/SC-ARM-19-028, 23 pp., www.arm.gov/publications/programdocs/doe-sc-arm-19-028.pdf.

——, H. Morrison, and E. Zipser, 2020: Effects of under-resolved convective dynamics on the evolution of a squall line. *Mon. Wea. Rev.*, **148**, 289–311, https://doi.org/10.1175/MWR-D-19-0187.1.

Velasco, I., and J. M. Fritsch, 1987: Mesoscale convective complexes in the Americas. *J. Geophys. Res.*, **92**, 9591–9613, https://doi.org/10.1029/JD092iD08p09591.

Verrelle, A., D. Ricard, and C. Lac, 2015: Sensitivity of high-resolution idealized simulations of thunderstorms to horizontal resolution and turbulence parametrization. *Quart. J. Roy. Meteor. Soc.*, **141**, 433–448, https://doi.org/10.1002/qj.2363.

Wang, D., M. Bartholomew, and E. Cromwell, 2018: Weighing Bucket Precipitation Gauge (WBPLUVIO2). ARM User Facility, accessed 27 December 2019.

Wilson, J. W., and R. D. Roberts, 2006: Summary of convective storm initiation and evolution during IHOP: Observational and modeling perspective. *Mon. Wea. Rev.*, **134**, 23–47, https://doi.org/10.1175/MWR3069.1.

Winker, D. M., J. L. Tuckett, B. J. Getzewich, Z. Liu, M. A. Vaughan, and R. R. Rogers, 2013: The global 3-D distribution of tropospheric aerosols as characterized by CALIOP. *Atmos. Chem. Phys.*, **13**, 3345–3361, https://doi.org/10.5194/acp-13-3345-2013.

Wulfmeyer, V., and Coauthors, 2008: The convective and orographically induced precipitation study. *Bull. Amer. Meteor. Soc.*, **89**, 1477–1486, https://doi.org/10.1175/2008BAMS2367.1.

Zelenyuk, A., and Coauthors, 2010: In situ characterization of cloud condensation nuclei, interstitial, and background particles using the single particle mass spectrometer, SPLAT II. *Anal. Chem.*, **82**, 7943–7951, https://doi.org/10.1021/ac1013892.

——, D. Imre, J. Wilson, Z. Y. Zhang, J. Wang, and K. Mueller, 2015: Airborne Single Particle Mass Spectrometers (SPLAT II & miniSPLAT) and new software for data visualization and analysis in a geo-spatial context. *J. Amer. Soc. Mass Spectrom.*, **26**, 257–270, https://doi.org/10.1007/s13361-014-1043-4.

Zhang, Y., and S. A. Klein, 2010: Mechanisms affecting the transition from shallow to deep convection over land: Inferences from observations of the diurnal cycle collected at the ARM Southern Great Plains site. *J. Atmos. Sci.*, **67**, 2943–2959, https://doi.org/10.1175/2010JAS3366.1.

Zhang, Z., A. C. Varble, Z. Feng, J. C. Hardin, and E. J. Zipser, 2021: Growth of mesoscale convective systems in observations and a seasonal convection-permitting simulation over Argentina. *Mon. Wea. Rev.*, https://doi.org/10.1175/MWR-D-20-0411.1, in press.

Zipser, E. J., D. J. Cecil, C. Liu, S. W. Nesbitt, and D. P. Yorty, 2006: Where are the most intense thunderstorms on Earth? *Bull. Amer. Meteor. Soc.*, **87**, 1057–1072, https://doi.org/10.1175/BAMS-87-8-1057.